https://doi.org/10.5194/egusphere-2026-2520
Preprint. Discussion started: 22 May 2026

Turbulence occurrence in the Tropical Tropopause Layer from superpressure balloon observations: distribution and sources

Flore JUGE [1,2], Richard WILSON [1], and Albert HERTZOG [3]

[1]Laboratoire Atmosphères, Observations Spatiales (LATMOS-IPSL), Sorbonne Université, Paris, France
[2]Centre national d'études spatiales (CNES), Paris, France
[3]Laboratoire de Météorologie Dynamique (LMD-IPSL), École polytechnique, Palaiseau, France

Correspondence: Flore JUGE (flore.juge@latmos.ipsl.fr)

Abstract. Turbulence characteristics remain poorly documented in the Tropical Tropopause Layer (TTL), although turbulence may play a significant role in the vertical transport of tracers and momentum from the troposphere to the stratosphere. In the framework of the Strateole-2 project, we use pressure, temperature and GPS *in situ* measurements collected under stratospheric Super-Pressure Balloons (SPBs) during long-duration flights at quasi-constant altitude (∼20 km) across the tropical belt. These quasi-Lagrangian observations are used to estimate high-resolution time series (∼110 s) of the gradient Richardson number (Ri), allowing us to characterize the flow regime, turbulent or laminar, along the balloon trajectories.

Using a classical instability criterion ($Ri < 0.25$), we estimate a mean turbulent fraction of about 0.18 in the tropical lower stratosphere and investigate its geographical variability. Turbulence occurrence is significantly enhanced in the vicinity of deep convection. Increased kinetic energy of short-period gravity waves is also observed close to convection, strongly suggesting that the breaking of gravity waves generated by convection constitutes an important source of turbulence in the TTL. We also identify turbulence events occurring far from convective regions, particularly over the Pacific Ocean, where they cluster in areas of enhanced vertical wind shear associated with the Quasi-Biennial Oscillation (QBO) amplified by the weakening with altitude of the upper branch of the Walker circulation.

These results highlight the important role of both convectively generated gravity waves and large-scale circulation patterns in controlling turbulence occurrence in the tropical lower stratosphere, with potential implications for tracer transport and mixing across the TTL.

1 Introduction

A major feature of the middle-atmosphere large-scale dynamics is the Brewer-Dobson meridional circulation (BDC), which is associated with an ascending branch in the tropics, poleward transport at mid-latitudes and subsidence at polar latitudes (Brewer, 1949; Butchart, 2014). The BDC ascending branch is notably responsible for the upward transport of tropospheric

https://doi.org/10.5194/egusphere-2026-2520
Preprint. Discussion started: 22 May 2026

species, such as water vapor (Plumb, 1996), and the tropical tropopause therefore constitutes the gateway to the whole middle atmosphere (Fueglistaler et al., 2009). Beyond the BDC, planetary and smaller-scale waves generated by deep convection also dynamically couple the troposphere and the stratosphere in the tropics (Andrews et al., 1987). Their upward propagation from convective sources and their breaking in the lower stratosphere eventually drive the Quasi-Biennial Oscillation (QBO) in tropical zonal winds (Fritts and Alexander, 2003; Jensen et al., 2016; Baldwin et al., 2001). In the tropical lower stratosphere, wave breaking either occurs due to the saturation of the wave amplitudes associated with the exponential decrease in atmospheric density or when waves encounter critical levels, i.e. when their ground-based phase speed approaches the background wind speed (Fritts and Alexander, 2003). Wave breaking is associated with the development of shear-driven instabilities, such as Kelvin–Helmholtz instabilities (KHIs), or convective instabilities, which act as efficient generators of small-scale turbulence and irreversible mixing (Dörnbrack, 1998; Fujiwara et al., 2003; Yamamoto et al., 2003; Mega et al., 2010).

Observational evidence from radar and aircraft measurements has shown that turbulence in the Tropical Tropopause Layer (TTL) often coincides with enhanced gravity wave activity and strong vertical wind shear, supporting the view that wave-induced instabilities play a key role in turbulent generation (Podglajen et al., 2017; Atlas and Bretherton, 2023). The breaking of larger-scale equatorial and planetary waves (Kelvin, inertio-gravity, mixed Rossby-gravity waves) has also been suggested as a contributor to turbulence and mixing near the tropical tropopause, highlighting the multiscale nature of wave–turbulence interactions in the tropical atmosphere (Dewan, 1981; Fujiwara et al., 2003; Fritts and Alexander, 2003).

Yet, turbulent sources in the tropical lower stratosphere are still poorly documented. A better characterization of these small-scale processes requires high-resolution observations, which are generally quite challenging to gather over the whole tropical band. Indeed, only sparse turbulence observations are available in the Tropical Tropopause Layer (TTL): most of them were collected by VHF Radars (Wilson et al., 2012; Luce et al., 2014), radiosondes (Atlas et al., 2025; Wilson et al., 2012; Luce et al., 2014) or aircraft measurements (Atlas and Bretherton, 2023; Podglajen et al., 2017). Radar and radiosonde datasets provide an Eulerian point of view on the atmospheric flow, with vertical profiles at specific locations. Information on turbulence can be extracted from such dataset with Thorpe analysis (Thorpe, 1977) using potential temperature profiles to identify turbulent instabilities (Wilson et al., 2011), or by estimating Richardson numbers from horizontal wind and temperature vertical profiles (Atlas et al., 2025). However, these data do not provide any information on the life cycle of turbulence patches.

We still lack a complete understanding of small-scale turbulent mixing in the Tropical Upper Troposphere and Lower Stratosphere (TUTLS), even though turbulence is involved in the global tracer and heat budgets. Given that the mean tropical upwelling is very slow, even weak turbulent mixing may be sufficient to compete with advection (Podglajen et al., 2017). Glanville and Birner (2017) have for instance analyzed the relative contributions of vertical advection, horizontal and vertical mixing to

https://doi.org/10.5194/egusphere-2026-2520
Preprint. Discussion started: 22 May 2026

transport in the tropical lower stratosphere, and have found that the contribution of vertical mixing could be as important as that of the vertical residual circulation.

These uncertainties in the quantification of turbulent mixing, which stem from both observational gaps and insufficient theoretical understanding, prevent reliable modelling of the TTL composition and limit our understanding of the processes that occur there. Conventional turbulence parameterizations that are used in current climate models are not very effective in stable stratification conditions in boundary layers (Mauritsen et al., 2007), such as those found in the lower stratosphere (Vanneste and Haynes, 2000; Alisse et al., 2000), and do not adequately represent the associated intermittent nature of turbulence in such conditions (Muñoz-Esparza et al., 2020; Flannaghan and Fueglistaler, 2011).

In this paper, we use Strateole-2 *in situ* measurements gathered from stratospheric long-duration balloons that fly at quasi-constant altitude to characterize turbulence occurrences in the tropical lower stratosphere. Such balloon flights provide quasi-Lagrangian measurements that follow the trajectory of air masses for several months, with a time resolution of 30 s. Further details on the different datasets used are given in Section 2. In Section 3, we describe a method to infer local gradient Richardson numbers (Ri) from the Strateole-2 observations, and use these numbers to estimate turbulent fractions along the balloon flights, and to study their geographical variations. In Section 4, we focus on turbulent events in the vicinity of convective systems and provide evidence for the role of high-frequency gravity waves to link deep convection with turbulence generation in the lower stratosphere. Finally, in Section 5, we explore turbulent events occurring away from deep convection, which we relate to background stability and shear conditions produced by large-scale circulations.

2 Datasets

2.1 Strateole-2 balloon-borne observations

Strateole-2 is an international project involving European and U.S. research groups, led by the Laboratoire de Météorologie Dynamique (LMD) and the Centre National d'Études Spatiales (CNES). The project aims to study atmospheric processes in the TUTLS using measurements collected along long-duration balloon flights.

The originality of this project lies in the use of closed superpressure stratospheric balloons (SPBs) filled with helium, which keep their volume nearly constant at flight level, and thus drift along constant-density surfaces for several months (Hertzog et al., 2007). Two flight levels are used during the project: the so-called 'TTL' and 'STR' levels, respectively corresponding to balloons flying at about 18.5 km and 20.5 km. The balloon diameter varies from one flight level to the other: 11 m for TTL flights and 13 m for STR flights. Drifting with the winds, SPBs can circle the globe following the flow and providing quasi-

https://doi.org/10.5194/egusphere-2026-2520
Preprint. Discussion started: 22 May 2026

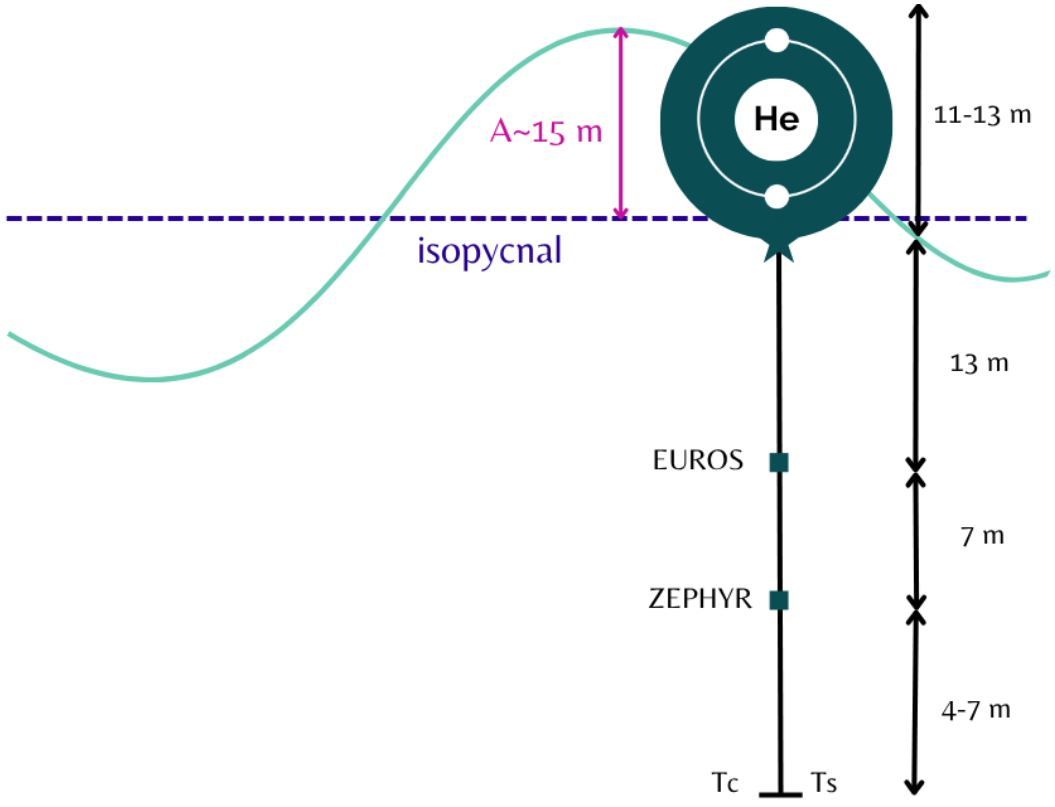

Figure 1. SPB general schematic. Two gondolas are suspended beneath the balloons: EUROS and ZEPHYR. Two temperature sensors (thermistor T_s and thermocouple T_c) are generally located several metres below the second gondola (ZEPHYR), except in the TTL3 configuration, where they are located next to EUROS gondola.
The distance between each component varies depending on the different configurations. The balloon diameter is set at 11 m for TTL flights and 13 m for STR flights.

Lagrangian measurements in the whole tropical band. Two separate gondolas are carried by the balloons: the first one, called EUROS, is suspended about 13 m below the balloon, while the second one, ZEPHYR, is hanging about 7 m below EUROS (Fig. 1). ZEPHYR is the payload gondola that hosts most of the instruments. Several configurations of this gondola are used, since the payload mass capacity is limited.

In this article, we focus on the TSEN (Thermodynamics SENsors) instrument, which is hosted in the EUROS gondola. This instrument provides observations of air temperature and pressure, as well as GPS measurements (Hertzog et al., 2007). It is carried on every Strateole-2 flight. The GPS receiver and the pressure sensor are located in the EUROS gondola, while the two temperature sensors, a thermistor and a thermocouple, are hanging several meters below the ZEPHYR gondola, separated by a rigid rod, 1 m apart (see Figure 1). Wind velocities derived from GPS and Pressure are representative of conditions at

https://doi.org/10.5194/egusphere-2026-2520
Preprint. Discussion started: 22 May 2026

Table 1. Characteristics of Strateole-2 flights, both campaigns.

Flights	Height (km)	Dates (UT)	Duration (day)
C0 (2019-2020)			
C0_01_STR1	20.65	12 Nov – 27 Feb	107
C0_02_STR2	20.50	11 Nov – 23 Feb	103
C0_03_TTL3	19.11	18 Nov – 28 Feb	101
C0_04_TTL1	18.78	27 Nov – 02 Feb	66
C0_05_TTL2	18.80	05 Nov – 23 Feb	79
C0_06_STR1	20.38	06 Dec – 01 Feb	57
C0_07_STR2	20.13	06 Dec – 28 Feb	83
C0_08_STR2	20.10	07 Dec – 22 Feb	77
C1 (2021-2022)			
C1_01_TTL5	18.47	19 Oct – 21 Oct	1
C1_02_STR1	20.21	20 Oct – 01 Nov	12
C1_03_TTL4	18.57	21 Oct – 21 Nov	31
C1_04_STR2	20.12	21 Oct – 19 Nov	29
C1_05_TTL3	18.49	27 Oct – 17 Dec	50
C1_06_TTL5	18.53	28 Oct – 11 Dec	43
C1_07_TTL4	18.52	01 Nov – 16 Dec	44
C1_08_STR1	20.31	05 Nov – 28 Dec	53
C1_09_STR2	20.24	06 Nov – 12 Jan	67
C1_10_TTL3	18.58	08 Nov – 16 Dec	38
C1_11_TTL1	18.55	08 Nov – 15 Dec	36
C1_12_STR4	20.46	12 Nov – 02 Jan	51
C1_13_STR1	20.37	15 Nov – 25 Jan	71
C1_15_TTL4	18.63	22 Nov – 18 Jan	56
C1_16_TTL5	18.51	22 Nov – 19 Dec	26
C1_17_TTL3	18.50	25 Nov – 16 Dec	20

balloon altitude. The temperature measurements (thermistor T_s, and thermocouple T_c) and GPS positions (longitude, latitude and altitude z_{GPS}) are recorded every 30 s. On the other hand, pressure measurements are performed every second.

Two Strateole-2 campaigns have been carried out from the Seychelles international airport (4.67°S, 55.52°E):

- **C0** : October 2019 to February 2020 (8 flights),
- **C1** : November 2021 to February 2022 (16 flights).

A final campaign (C2) is scheduled during the 2026 boreal autumn. The main characteristics of the flights performed during the C0 and C1 campaigns (*i.e.*, ZEPHYR configuration, mean height level, dates and durations) are presented in Tab.1.

The trajectories of Strateole-2 flights are displayed in Figure 2, with C0 flights in green and C1 flights in purple. The balloons mostly flew within ±10° of the equator. Both the C0 and C1 campaigns correspond to the end of a positive phase of the QBO, *i.e.*, eastward winds at the balloon flight levels and westward winds above. Consequently, the Indian and Pacific oceans as well as the Maritime Continent were well sampled during both campaigns. Yet, the zero-wind line was located closer to the balloon

https://doi.org/10.5194/egusphere-2026-2520
Preprint. Discussion started: 22 May 2026

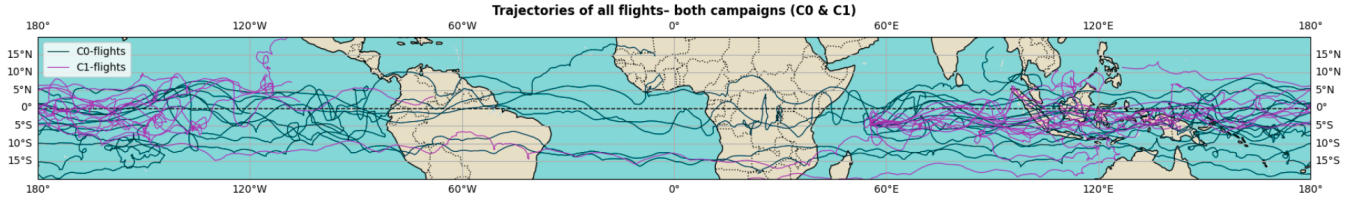

Figure 2. Trajectories of all flights from Strateole-2 C0 (2019) and C1 (2021) campaigns.

flight levels during C1 than during C0. On the other hand, South America, the Atlantic Ocean and Africa were relatively less sampled, especially during the second campaign. During that campaign, issues affecting the balloon envelopes actually limited the flight duration, sometimes preventing the balloons from reaching America. Also, the eastward background winds were starting to shift to westward winds at the end of C1, and some balloons even reversed direction over the Pacific Ocean (Corcos et al., 2025).

2.2 GPM-MERGIR dataset: location of convective cells

Among the possible mechanisms causing turbulence in the TTL are instabilities induced by gravity waves, some of which may be generated by convective systems. To study the link between deep convection and turbulence occurrences, we have used the spaceborne GPM-MERGIR dataset (Janowiak et al., 2017).

GPM-MERGIR is a global merged infrared (IR) dataset: it combines infrared measurements from geostationary satellites to produce global maps of brightness temperature T_b (used as a proxy for infrared cloud-top emission) between approximately 60 °S and 60 °N. The images have a spatial resolution of 4 km, and a temporal resolution of 30 min (Janowiak et al., 2017). The dataset is intended to provide near-global coverage, including areas without surface instruments, making it a useful tool for analysing phenomena such as convective systems and cloud cover. In this paper, the GPM-MERGIR brightness temperatures are used to estimate the distance between the Strateole-2 balloons and nearby convective cells, along their trajectories.

Figure 3 shows maps of brightness temperature, centered around the balloon location at two different times during the second flight of the C1 campaign. Deep convection is assumed to occur if $T_b < 230$ K. For each balloon position record, we estimate the distance between the balloon and the closest convective cell in the GPM-MERGIR dataset at the same time.

2.3 ERA-5

In the following, we will use the ERA-5 reanalysis (Hersbach et al., 2020) to provide information on mesoscale dynamics, stability conditions and atmospheric waves in the vicinity of the balloon position.

https://doi.org/10.5194/egusphere-2026-2520
Preprint. Discussion started: 22 May 2026

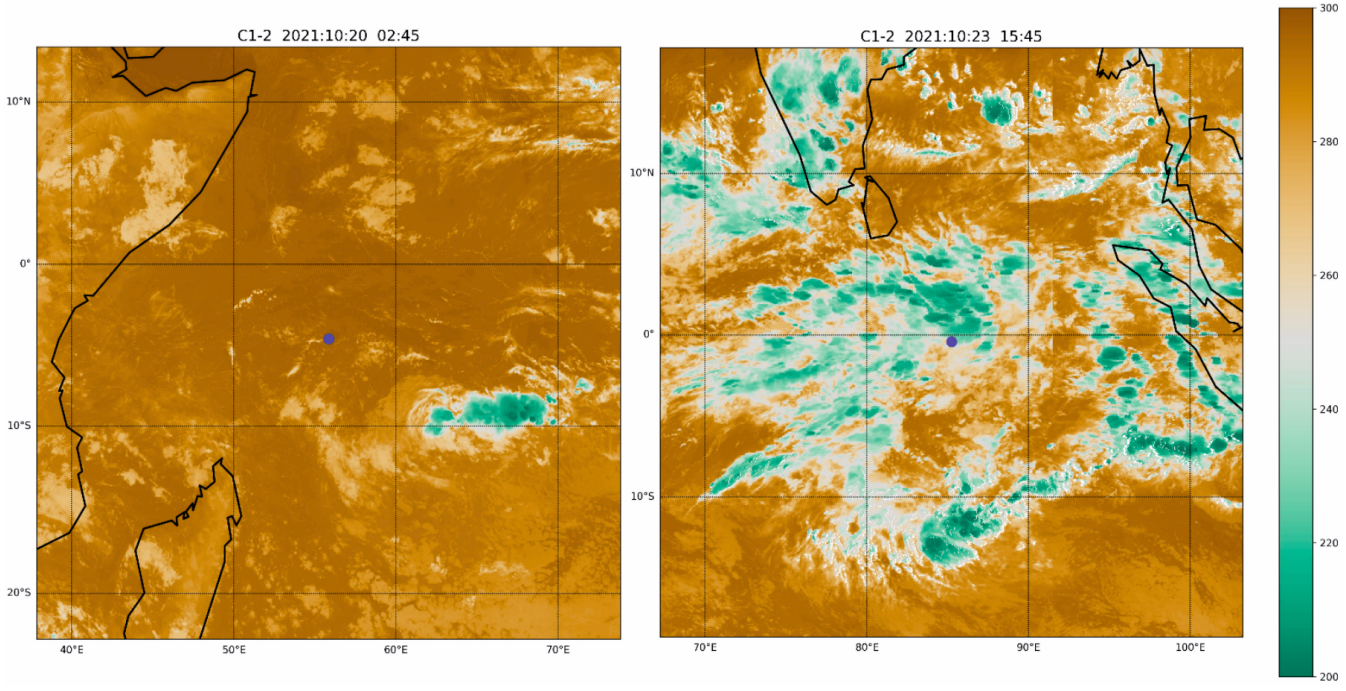

Figure 3. Satellite images (from GPM-MERGIR data) centred on the balloon position (purple point) at different moments during flight 2, C1. The color bar represents the brightness temperature T_b in Kelvins.

ERA-5 reanalysis is produced by the European Centre for Medium-Range Weather Forecasts (ECMWF). ERA-5 provides a consistent representation of the global atmosphere by assimilating a large set of observations into a numerical forecast model. Here, we use a 0.25° × 0.25° spatial and a 6-hour temporal resolution, covering the whole planet.

In this article, the horizontal wind velocities, temperatures, and geopotential height at the 100, 70, and 50 hPa pressure levels are used, corresponding to the upper troposphere and lower stratosphere. These fields are extracted between 5°N and 5°S to focus on equatorially-trapped waves. Although ERA-5 does not resolve small-scale convective or turbulent processes, including high-frequency gravity waves, its large-scale fields provide a robust reference for synoptic analysis and for estimating background stability and shear conditions.

3 Detection of turbulent patches in Strateole-2 balloon time series

3.1 Richardson number estimates from Strateole-2 TSEN measurements

From the TSEN pressure (P) and temperature (T) raw measurements, we can compute the potential temperature θ, density ρ, vertical displacements between successive measurements δz_P using the hydrostatic balance and the ideal gas law. Horizontal

https://doi.org/10.5194/egusphere-2026-2520
Preprint. Discussion started: 22 May 2026

wind velocities (zonal u, meridional v) are derived from GPS positions by centered finite differences.

$$\theta = T\left(\frac{P_0}{P}\right)^{\frac{R_a}{c_p}}, \qquad \rho = \frac{P}{R_a T}, \qquad \delta z_P = -\frac{\delta P}{\rho g} \tag{1}$$

where $g = 9.8$ m.s^{-2} is the gravitational acceleration, $R_a = 287$ J.kg^{-1}.K^{-1}, is the specific dry air constant, and $c_p = 1004$ J.kg^{-1} is the isobaric heat capacity.

Since superpressure balloons (SPB) drift in a stratified environment, they oscillate vertically about their constant-density equilibrium position, with gravity and buoyancy acting as restoring forces. Figure 4 shows two samples of balloon observations. SPB vertical oscillations about their equilibrium level are clearly visible in the upper panel. These oscillations have typical periods between 3 and 4 min, *i.e.*, slightly shorter than the local Brunt-Väisälä period (Vincent and Hertzog, 2014). Wilson et al. (2023) presented the probability distribution of these periods for the C0-campaign. They exhibit a mode near 220 s, which typically corresponds to seven or eight 30-s (u, v, T) datapoints per period. The amplitude of these oscillations varies during the flight and typically ranges between a few meters and a few tens of meters, with a mean around 15 m (*i.e.* peak-to-peak amplitude $\overline{|\Delta z|} = 30$ m).

These vertical oscillations induce fluctuations in any balloon-borne measurements. This is illustrated, for instance, in the middle panel of Figure 4 for potential temperature. In this study, we will use these balloon oscillations around their equilibrium density level as short vertical profiles in order to estimate local vertical gradients of any measured variable X (u, v, T, or θ). Specifically, to estimate the gradients, successive altitude relative extrema are first identified in the balloon time series, and associated with the corresponding values of the measured variables X at the same time. From the successive altitude extrema, algebraic altitude increments Δz_P are computed with an effective temporal resolution of about 110 s (a half-oscillation period). ΔX increments are computed similarly. Finally, the ratio of these increments provides an estimate of the vertical gradient:

$$X_z = \frac{\Delta X}{\Delta z} \tag{2}$$

We refer to this method as the envelope method. The envelopes of the balloon vertical displacements and potential temperatures are for instance color-filled in Figure 4.

From these gradients, estimates of the Brunt-Väisälä frequency (N^2) and of the squared vertical wind shear (S^2) can be derived:

$$N^2 = \frac{g}{\bar{\theta}}\frac{\partial \theta}{\partial z} = \beta_\theta \frac{\partial \theta}{\partial z} \qquad S^2 = \left(\frac{\partial u}{\partial z}\right)^2 + \left(\frac{\partial v}{\partial z}\right)^2 \tag{3}$$

https://doi.org/10.5194/egusphere-2026-2520
Preprint. Discussion started: 22 May 2026

where $\beta_\theta = \frac{g}{\theta}$ is the buoyancy parameter. The ratio of these two quantities finally gives an estimate of the gradient Richardson number Ri, which enable us to characterize the flow as laminar or turbulent:

$$Ri = \frac{N^2}{S^2} \tag{4}$$

Times series of Ri are obtained accordingly along each flight with a relatively high time resolution (around 110 s).

The lower panel of Figure 4 for instance, shows the estimated vertical gradient of potential temperature with the envelope method for the two balloon samples. In the left panel, z_P and θ fluctuate mostly in phase, as expected under stable stratification ($\partial_z\theta > 0$). In this case, the deduced vertical gradient of potential temperature is generally positive and typically associated with large Richardson numbers. In contrast, in the right panel, the two signals partially lose phase coherence and may even become anti-correlated, indicative of locally weakened stratification or neutral to unstable conditions ($\partial_z\theta \leq 0$). This scenario corresponds to reduced N^2 and may imply low or negative Richardson numbers. Such conditions are typically associated with shear instabilities and turbulence.

In the following, we will consider that the flow is turbulent as soon as $Ri < 0.25$ (Miles, 1961; Howard, 1961), and is laminar otherwise. This Richardson number criterion is theoretically only valid for plane-parallel flow and its use in the real three-dimensional atmosphere has been discussed in the literature. It has, for instance, been questioned in simulations (Achatz, 2005) as well as in observations (Balsley et al., 2008). Hines (1988) even proposed a slantwise static instability as a mechanism for producing turbulence. Haack et al. (2014) directly detected 15-130 m thick turbulent layers in the stratosphere using wind fluctuations measured by a very high resolution balloon-borne instrument (LITOS). They have shown that among the detected turbulent layers, some coincide with estimates of $Ri > 0.25$, regardless of the scale used to estimate Ri, although a good correlation is found between $Ri < 0.25$ and turbulence occurrences. This critical threshold seems to be a useful indicator of turbulence in general, even though it is not a necessary condition to observe atmospheric turbulence: active turbulence might actually occur for Ri larger than this threshold, typically up to values of $Ri \sim 1$ (Woods, 1969; Stull, 1988; Galperin et al., 2007). In the range $0.25 < Ri < 1$, the flow may thus either be turbulent or laminar. We nevertheless favor a conservative approach in this paper, so that our estimates should provide a lower bound for turbulence occurrences in the tropical UTLS.

Yet, our Ri estimates come with uncertainties that are related to those of the measurements performed onboard the balloons. The relative uncertainty of Ri estimates is derived in Appendix A:

$$\frac{\delta Ri}{Ri} \approx \sqrt{\left(\frac{\delta\Delta\theta}{\Delta\theta}\right)^2 + 4\left(\frac{\delta\Delta u}{\Delta u}\right)^2 + 4\left(\frac{\delta\Delta v}{\Delta v}\right)^2 + 9\left(\frac{\delta\Delta z}{\Delta z}\right)^2} \tag{5}$$

https://doi.org/10.5194/egusphere-2026-2520
Preprint. Discussion started: 22 May 2026

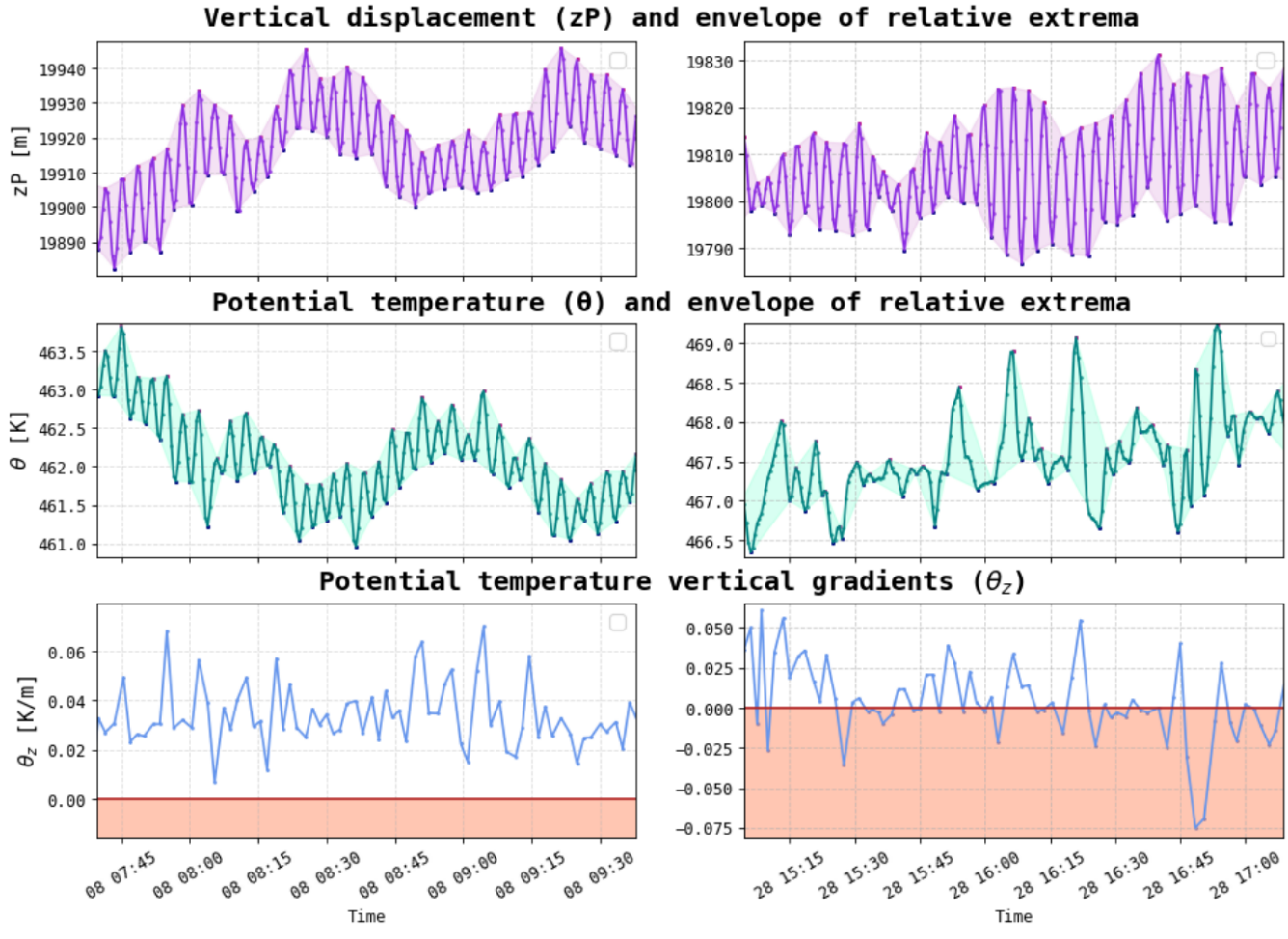

Figure 4. Time series of balloons vertical oscillations and envelopes (up), corresponding potential temperature fluctuations and envelopes (middle), and associated vertical gradients (down) from flight 8, C0. The red lines show the threshold of unstable potential temperature gradient ($\theta_z = 0$). The left panels correspond to a period of stable conditions, and right ones, to unstable conditions.

https://doi.org/10.5194/egusphere-2026-2520
Preprint. Discussion started: 22 May 2026

Using representative background values for static stability $\langle N^2 \rangle$ and for wind shear $\langle S^2 \rangle$, the standard deviation of δRi (σ_{Ri}) can furthermore be expressed as:

$$\sigma_{Ri} \approx \frac{1}{|\Delta z|} \frac{\langle N^2 \rangle}{\langle S^2 \rangle} \sqrt{2(\sigma_\theta)^2 \cdot \left(\frac{\beta_\theta}{\langle N^2 \rangle} \right)^2 + 18(\sigma_z)^2 + 16 \frac{(\sigma_{u,v})^2}{\langle S^2 \rangle}} \tag{6}$$

where σ_z, $\sigma_\theta \approx \theta / T \sigma_T$, $\sigma_{u,v}$ respectively are the standard deviations of the uncertainties in the altitude estimates (Equation (1)), the potential temperature and the wind measurements.

Equation (6) notably shows that the standard deviation of Ri estimates is inversely proportional to the amplitude of the balloon oscillations. This can be understood intuitively since, for small-amplitude oscillations, both increments in the envelope method (Δz_p and ΔX) will be small, and therefore more sensitive to measurement uncertainties. More specifically, the estimate of $\Delta X = X_z \Delta z$ could be such that $X_z \Delta z_p \ll \sqrt{2} \sigma_X$. On the other hand, for large balloon oscillations, the increments are dominated by the atmospheric gradients, and the Ri estimates become more reliable.

In addition, we note that there exists a significant difference between daytime (Solar Zenith Angle, or SZA$< 94°$) and nighttime (SZA$\geq 94°$) uncertainties in temperature measurements. Daytime standard deviations are typically larger by a factor 3 to 5 than during nighttime conditions (e.g., Wilson et al., 2023). Indeed, during daytime, the temperature sensors are heated by solar radiation and become warmer than the ambient air. The solar radiation can also create artificial temperature anomalies when the sensors cross the (warm) wake of devices in the flight chain. A similar, though much smaller (20% increase), diurnal variation has been observed in the uncertainty of pressure observation (Wilson et al., 2023). Last, as already mentioned, the temperature sensors are located very close to the EUROS gondola in the TTL3 configuration. They are therefore exposed to stronger wake perturbations, so that the temperature measurements for the TTL3-flights are by far the noisiest cases (Wilson et al., 2023). We consequently exclude those flights from the following analysis.

3.2 Turbulent fraction estimates

3.2.1 Methodology and sensitivity to Δz

To further illustrate the sensitivity of Ri estimates to the amplitude of the balloon oscillations, we show in Figure 5 the probability distribution of Ri for three different bins of $|\Delta z|$.

It can be seen that the conditional probability of observing a Ri lower than 0.25 increases with smaller oscillation amplitudes. In the 0-10 m $|\Delta z|$ bin, this probability even reaches 50%. Actually for very small $|\Delta z|$, the increments are dominated by the

https://doi.org/10.5194/egusphere-2026-2520
Preprint. Discussion started: 22 May 2026

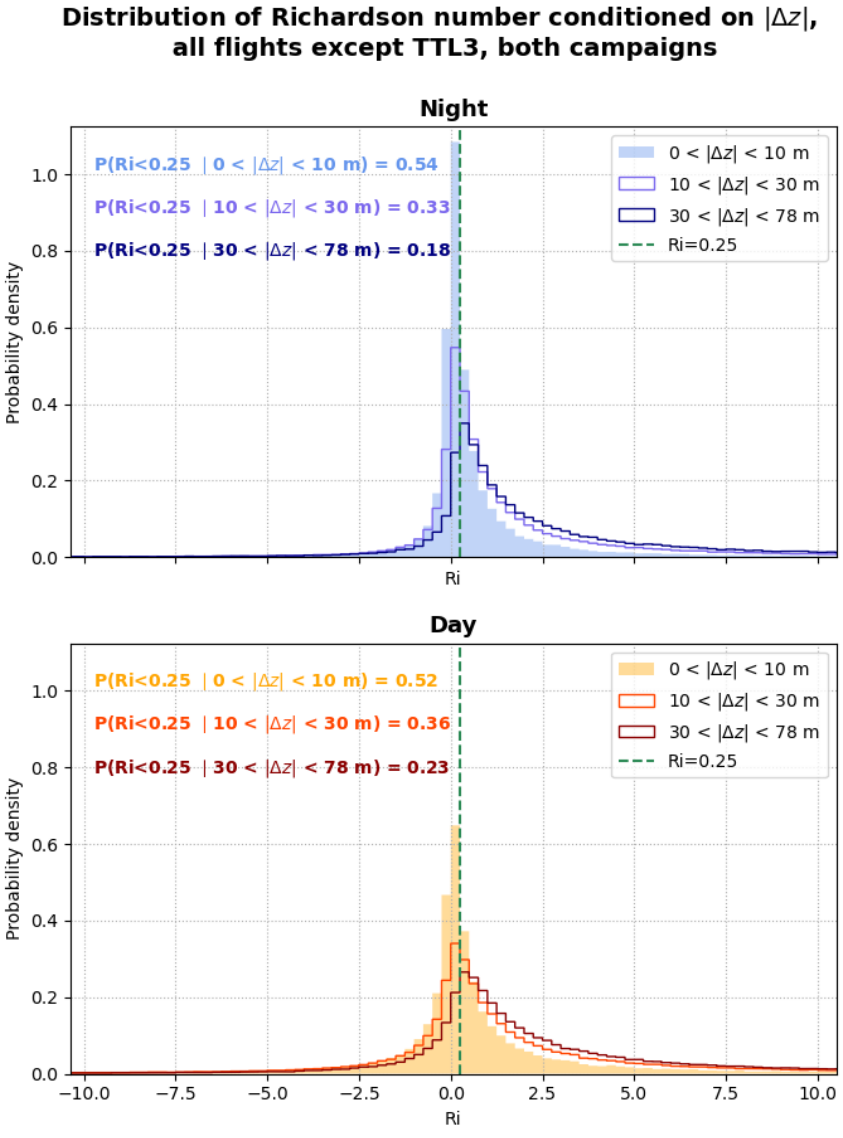

Figure 5. Empirical Probability Density Function (PDF) of Richardson number estimates for 3 classes of balloon vertical oscillations amplitudes, for nighttime (top) and daytime data (bottom), all flights except TTL3, both campaigns. The green vertical dashed lines represent the threshold of sub-critical Ri.

observational noise, so that the probability to observe positive or negative $\Delta\theta$ are nearly equal (see Figure A1 in Appendix A). It is therefore very difficult to directly estimate the relative uncertainty in Ri for small Δz. In contrast, when the oscillation

https://doi.org/10.5194/egusphere-2026-2520
Preprint. Discussion started: 22 May 2026

amplitudes increase, the Ri distributions become more skewed toward positive values. In any case, the mode of the distribution remains close to the 0.25 threshold.

In the following, we will define the mean turbulent fraction ($\bar{F}$) as the probability of $Ri < 0.25$, i.e., the ratio of the number of $Ri < 0.25$ estimates (n_{turb}) to that of the total number of estimates (n_{tot}):

$$\bar{F} = P[Ri < 0.25] = \frac{n_{turb}}{n_{tot}} \tag{7}$$

The relative uncertainty in Ri, which depends on the amplitude of balloon oscillations, may significantly affect the estimation of the turbulent fraction. Indeed, to estimate this fraction, the key factor is the quantity of small Ri values that are close to the subcritical threshold (0.25), *i.e.* Ri values corresponding to the mode of the distribution as shown in Figure 5. This mode, and thus the detected turbulent fraction, is found to be dependent on the amplitude of the balloon's oscillations for small amplitudes. We therefore consider the amplitude of the oscillations to be a key factor in estimating the flow characteristics: the turbulent fraction (and its uncertainty) is then more accurately estimated when the amplitude of the SPB oscillations is larger. Regarding the uncertainty, the background stability and shear values that appear in Equation (6) are therefore estimated using only the largest-amplitude oscillation class ($|\Delta z|$ >30 m). We obtain values of $\langle N^2 \rangle = 4.1 \times 10^{-4}$ rad.s^{-2} and $\langle S^2 \rangle = 4.5 \times 10^{-4}$ s^{-2}, which are consistent with typical values in the tropical lower stratosphere.

3.2.2 Turbulent fraction estimates from Strateole-2 observations

The conditional probabilities of turbulence occurrences ($Ri < 0.25$) as a function of balloon-oscillation amplitude ($|\Delta z|$) are displayed in Figure 6. The colored shading around each curve indicates the uncertainty in the estimation of the turbulence fraction, *i.e.* the probability that $Ri \pm \sigma_{Ri}$ is smaller than 0.25 in each $|\Delta z|$ class. The uncertainty is greater for daytime data, because a large part of the uncertainty in Ri is associated with the uncertainty in the temperature observations (σ_θ in equation 6), as mentioned in the previous section. As the uncertainty in Ri decreases with increasing amplitude of the balloon oscillations, the turbulent fraction estimates are accordingly more constrained for large $|\Delta z|$.

The lower panel of Figure 6 exhibits the number of daytime and nighttime samples considered in each $|\Delta z|$ class. We can observe that the balloon oscillations tend to have larger amplitudes during daytime than during nighttime. This might be associated with the heating of the balloon envelope during day which expands the gas inside the balloon and tends to slightly increase the amplitude of their vertical motions.

https://doi.org/10.5194/egusphere-2026-2520
Preprint. Discussion started: 22 May 2026

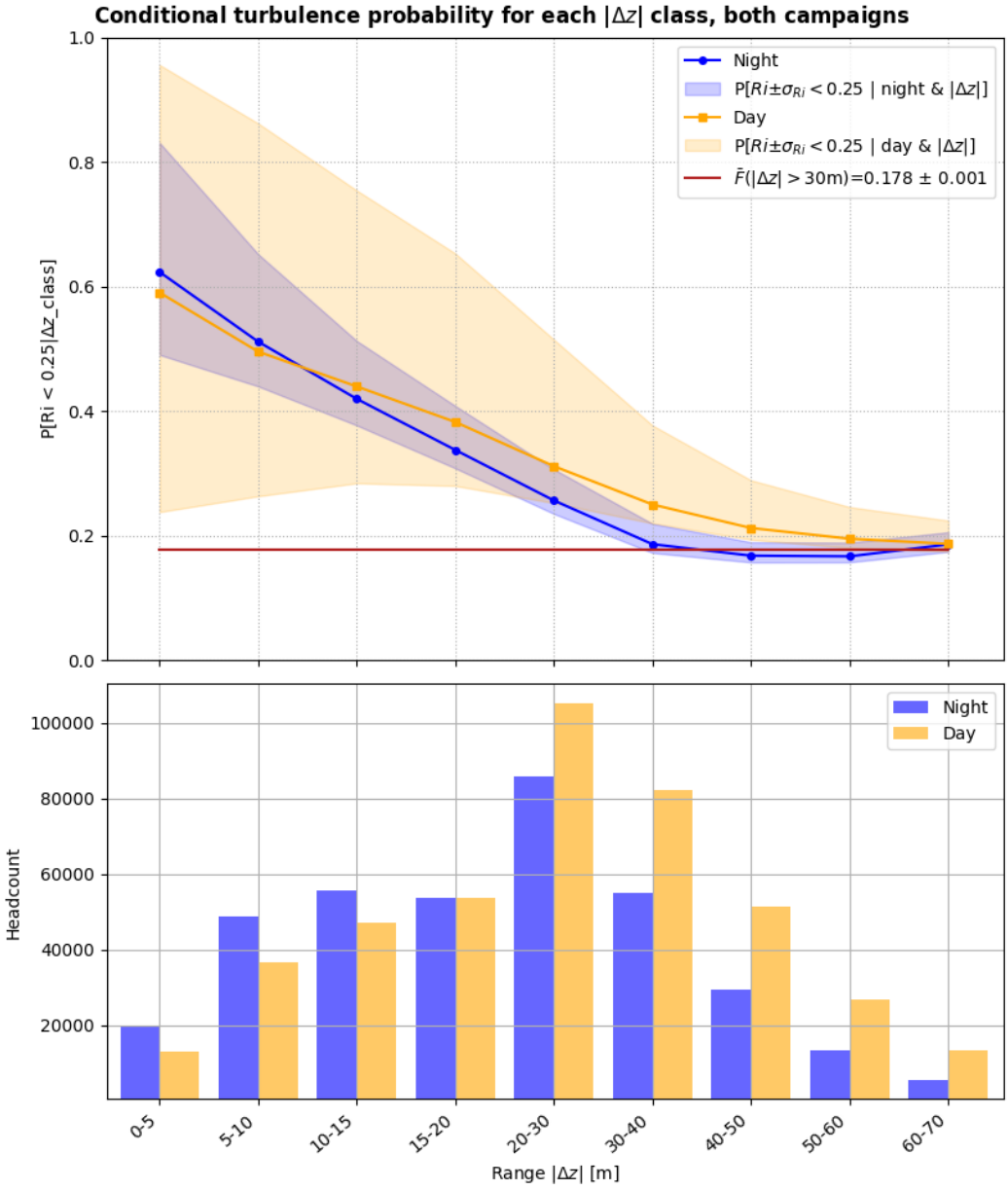

Figure 6. Conditional turbulence probabilities for each $|\Delta z|$ class during daytime (orange) and nighttime (blue), all flights of both campaigns (upper panel). The colored areas represent the interval for which $Ri \pm \sigma_{Ri} \leq 0.25$. The red line corresponds to the mean turbulent fraction estimated over all the data associated with $|\Delta z| > 30$ m. The lower panel shows the headcounts for daytime and nighttime data in each $|\Delta z|$ class.

The top panel of Figure 6 shows that both the daytime and nighttime conditional probability of turbulence fraction decrease with increasing $|\Delta z|$ up to 30 m, and become fairly constant afterwards. The turbulent fraction decrease first highlights that the

https://doi.org/10.5194/egusphere-2026-2520
Preprint. Discussion started: 22 May 2026

noise level in the measurements dominates the estimates of the vertical gradients when $|\Delta z| < 30$ m, so that it is not possible to reliably estimate the Richardson number for those small oscillation amplitudes. In contrast, it is noteworthy that the turbulent fraction becomes quasi-independent of the amplitude of the balloon vertical oscillations when $|\Delta z| > 30$ m. This suggests that these estimates are robust. The "large-oscillation" situations represent about half of the total dataset (see lower panel in Fig. 6). Our estimates of the turbulent fraction in the tropical lower stratosphere from the Strateole-2 dataset are therefore 0.178 ± 0.001 and 0.225 ± 0.001 for nighttime and daytime data respectively.

Those estimates are at the high end of the range of estimates found in the literature for the lower stratosphere. Atlas et al. (2025) recently used a 21-years database of radiosounding vertical profiles in the equatorial UTLS with a vertical resolution of 200 m to estimate Richardson numbers between 20 and 30 km. They computed turbulent fractions for different phases of the QBO. The turbulent fraction estimated for the QBO positive phase (eastward background winds) was $\sim$0.5%, and the one associated with the transition from positive to negative phase was $\sim$1%. These values are therefore more than one order of magnitude lower than our estimates. Yet, an important difference between our two studies is the vertical scale at which the Richardson numbers are estimated : 200 m in Atlas et al. (2025) vs 30 to 70 m here. Indeed, Balsley et al. (2008) showed that Ri estimates depend on the scale at which they are computed, and consequently, turbulent fractions as well.

In contrast, Alisse et al. (2000) found a mean turbulent fraction of ~ 0.18 using very high vertical resolution (1 m) balloon sounding data, in the mid-latitude lower stratosphere (11-23 km). This estimate is much closer to our estimate, even though it corresponds to different latitudes.

We note in addition that, in those two studies, the turbulent fraction estimates represent an average over a large range of altitudes, typically the whole lower stratosphere, whereas our estimates are representative of a narrow vertical range ($\lesssim 2$ km).

3.2.3 Geographical differences in the turbulent fraction estimates

In order to describe the spatial variability of the turbulent fraction, the turbulence statistics have been estimated for six different geographical areas. The boundaries of these areas are detailed in Table 2.

Region	Longitudes [°]
Pacific ocean	(180, -80)
America	(-80, -40)
Atlantic ocean	(-40, 10)
Africa	(10, 50)
Indian ocean	(50, -91)
Maritime continent	(91, 180)

Table 2. Characteristics of geographical boxes.

https://doi.org/10.5194/egusphere-2026-2520
Preprint. Discussion started: 22 May 2026

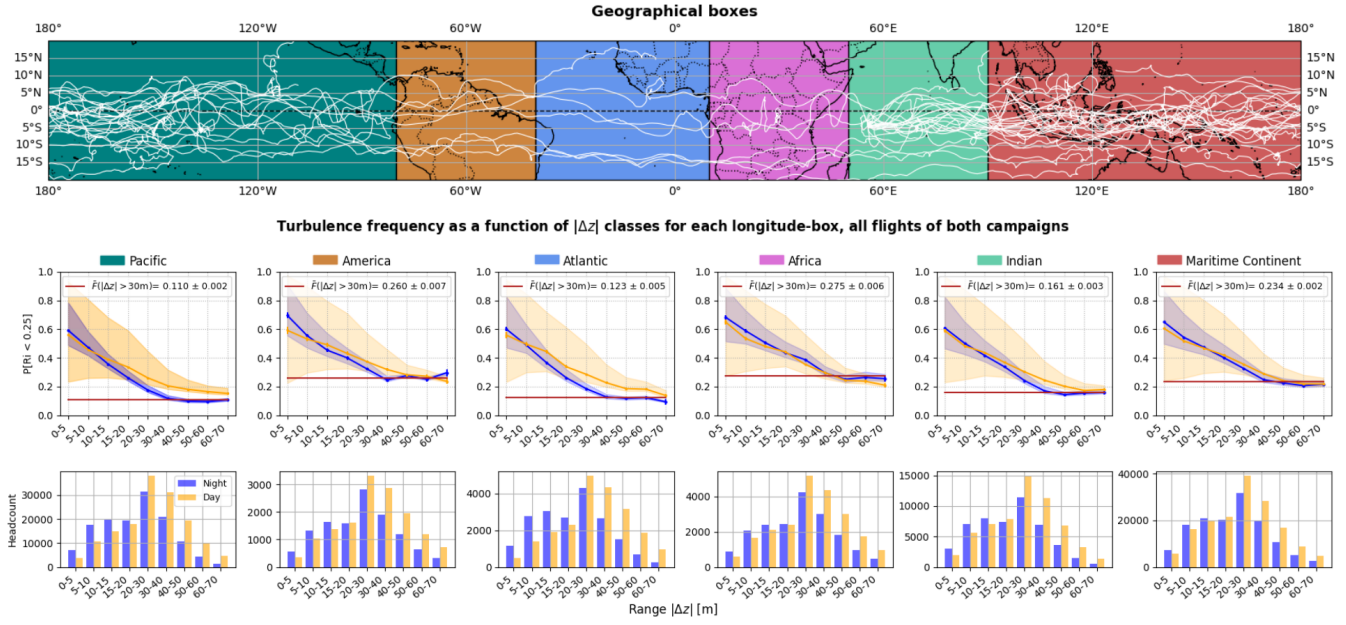

Figure 7. Turbulence detection probability for different geographical regions as a function of balloon-vertical-oscillation amplitudes, both campaigns. The first panel exhibits the 6 geographical region boundaries and the trajectories of all Strateole-2 flights. The second and third panels are the same as in Figure 6, but according to the different regions.

Figure 7 exhibits the regional differences in the distribution of detected turbulent events. The top panel shows the trajectories of all flights used from both Strateole-2 campaigns, except TTL3-flights. The colored areas correspond to the six regions used to evaluate the geographical differences: Pacific Ocean, South America, Atlantic Ocean, Africa, Indian Ocean and Maritime Continent. The middle panel shows the conditional turbulence probability in each $|\Delta z|$ class, as before, for both daytime and nighttime conditions, but estimated in these six different geographical regions. The lower panel displays the headcounts of data for both daytime and nighttime in each class of $|\Delta z|$ amplitude for each region.

Figure 7 first shows that, as expected, the dependence of turbulent fraction estimates on $|\Delta z|$ is fairly similar in all geographical regions. In particular, as soon as $|\Delta z| \geq$30 m, the turbulent fraction estimates remain nearly constant, as indicated by the red horizontal lines in the middle panel. We interpret this behaviour at large oscillation amplitudes as evidence for a robust estimation of the turbulent fraction.

However, the level of the plateau beyond 30 m varies from one region to another. We note that the turbulent fraction is larger over continental regions (Africa, America) and the Maritime Continent, with values ranging from 0.23 over the Maritime Continent to 0.275 over Africa, than over oceans (Atlantic, Pacific and Indian oceans), with values ranging from 0.11 over the

https://doi.org/10.5194/egusphere-2026-2520
Preprint. Discussion started: 22 May 2026

Pacific to 0.16 over the Indian Ocean. The standard errors of these probabilities are about a few 10^{-3} for both campaigns taken together, with slightly larger values over South America, the Atlantic Ocean, and Africa due to reduced sampling.

Among the oceanic basins, the Indian Ocean stands out as the region with the largest mean turbulent fraction. But if we analyze the two campaigns separately, we can note significant differences in the turbulent fraction: 0.13 ($\pm 4.4 \times 10^{-3}$) during C1, which is quite close to the values estimated for the Pacific and the Atlantic oceans, and 0.19 ($\pm 4.8 \times 10^{-3}$) during C0, which is substantially larger in comparison. Actually, during the C0-campaign in 2019, an historically strong positive phase of the Indian Ocean Dipole (IOD) took place (Lu and Ren, 2020), with strong positive sea surface temperature anomalies in the western Indian Ocean basin. By weakening the climatological (positive) west–east convection gradient across the whole basin (Saji et al., 1999), this positive IOD event led to a more balanced spatial distribution of convective activity in the basin (Corcos et al., 2021). According to Muhammad et al. (2019), a positive IOD event also leads to enhanced Kelvin wave (KW) and Mixed Rossby–Gravity wave (MRGW) activity over Eastern Africa and Southern Indian Ocean, and weakened wave activity over the Eastern Indian Ocean and the Maritime Continent. The observed difference in the turbulence fraction between the two Strateole-2 campaign may therefore reflect the variation of the IOD index between 2019 and 2021.

The geographical boxes do not contain the same number of data points. America, Atlantic and Africa are under-represented in comparison with the other regions, especially for the second campaign (C1). We nevertheless notice that the turbulent fraction estimates do not seem to depend on the number of points. Indeed, we observe regions that are densely sampled with either low (Pacific Ocean) or high (Maritime Continent) turbulent fractions, and conversely, sparsely sampled regions with low (Atlantic Ocean) or high (Africa and South-America) turbulent fractions. Thus, the inter-regional sampling differences do not seem to strongly affect the turbulent fraction estimates.

4 Turbulence and deep convection

4.1 Geographical distribution of turbulent events and their proximity to convection

The previously reported geographical differences in turbulent fraction seem to be fairly consistent with the geographical distribution of tropical deep convection. In order to better understand the link between turbulence detections and underneath convection, we make use in this section of the GPM-MERGIR dataset to classify turbulence detections according to their distance to convective systems.

https://doi.org/10.5194/egusphere-2026-2520
Preprint. Discussion started: 22 May 2026

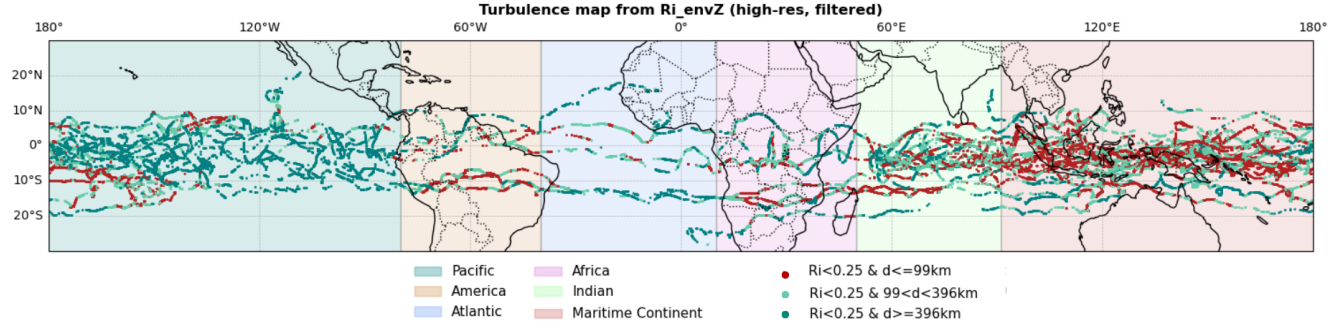

Figure 8. Map of detected turbulent events with colors corresponding to 3 equiprobable classes of minimum distance between the balloons and the convective systems (d), all flights except TTL3 ones, both campaigns. The colored areas correspond to the different geographical regions.

Figure 8 presents all the valid turbulence detections for both campaigns, *i.e.* $Ri < 0.25$ and $|\Delta z| > 30$ m. Each dot represents a turbulent event and its color corresponds to a distance class. We have chosen to use three equiprobable classes of distance, *i.e.* containing the same number of observations: 0-99 km (firebrick), 99-396 km (seagreen), and >396 km (dark cyan).

The turbulent events occur everywhere in the tropical belt, but it can be seen that most events associated with nearby convection (red points) are clustered over the Maritime Continent, while some appear over South America, Africa and Indian Ocean. Very few are observed over the Pacific and the Atlantic Ocean. The link between deep convection in the troposphere and lower-stratosphere turbulence may stem from the propagation and breaking of high-frequency gravity waves (HF-GWs) triggered by convection, which propagate nearly vertically upward. This hypothesis will be examined in the next sections. Over the central and eastern Pacific and the Atlantic oceans, on the other hand, most of the turbulent events are detected far from deep convection: this aspect will be investigated in the last section of the paper.

4.2 Turbulent density and distance to convection

To obtain more quantitative insights into the relationship between turbulent events and proximity to convective systems, we define a metric of turbulence occurrence over a data segment of duration $\Delta t = 3$ h as:

$$TD_{\Delta t=3\mathrm{h}} = \frac{n\big(Ri < 0.25 \text{ and } |\Delta z| > 30\,\mathrm{m}\big)}{n\big(|\Delta z| > 30\,\mathrm{m}\big)} \tag{8}$$

https://doi.org/10.5194/egusphere-2026-2520
Preprint. Discussion started: 22 May 2026

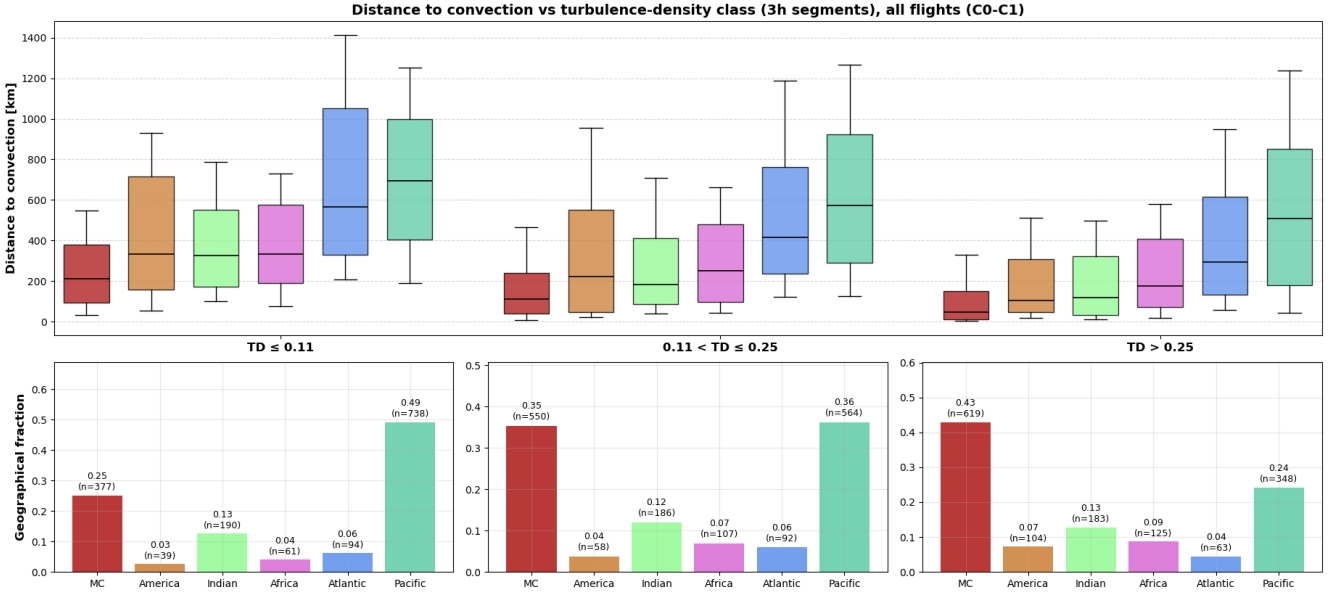

Figure 9. (The upper panel shows the averaged minimal distance to convection estimated on 3h-segments per class of turbulent density, for each region, all flights of both campaigns. The whiskers represent the 10th and 90th percentiles and black lines, the medians of distributions. The lower panel exhibits the fraction of data in each TD-class corresponding to each region.

where TD denotes the turbulent density, and $n(\cdot)$ is the number of observations satisfying the above conditions in the 3 h data segment. In the following, we use only segments for which $n(|\Delta z| > 30\,\mathrm{m}) > 30$ to avoid quantification issues and ensure statistically meaningful estimates.

We also compute the average of the balloon distance to convection on the same 3 h-segments.

The upper panel of Figure 9 represents boxplots of this average distance for each geographic region and for three equiprobable classes of turbulent density. The boxes show the 25th and 75th percentiles while the whiskers correspond to the 10th and 90th percentiles, and the horizontal black lines are the medians of the distributions. Regardless of the geographical region considered, Figure 9 exhibits a general tendency toward shorter distances to convection for higher turbulence densities, supporting a clear relationship between stratospheric turbulence and underneath convection. This is true for both the median and 90th percentile distance. On the other hand, the 10th percentile distance does not show any significant variation with the turbulent density class, indicating that laminar flows can also be observed close to convection.

It can also be noted that the balloon distance to convection is systematically lower over the Maritime Continent than over the other regions, whatever the turbulence density class. Indeed, the balloons are very often in the vicinity of a convective system over the Maritime Continent, which is also the region where gravity-wave momentum fluxes reach their maximum in the Strateole-2 dataset (Corcos et al., 2021).

https://doi.org/10.5194/egusphere-2026-2520
Preprint. Discussion started: 22 May 2026

The second panel of Figure 9 displays, for each turbulent density class, the share of each geographical region in terms of data points in that class. The panel notably shows that more than 40% of the segments with the highest turbulent densities are located over the Maritime Continent, and that, on the other hand, nearly 50% of the lower turbulent density data segments are found over the Pacific Ocean. Continents also have a larger share in the higher turbulent density class than in the lower one.

4.3 Role of high-frequency gravity waves

4.3.1 HF-GW Kinetic energy estimates

The previous results suggest a link between deep convection in the tropical troposphere and turbulence occurrences in the lower stratosphere. Yet, deep convection very rarely reaches altitudes at which the balloons are flying, so that we now investigate whether high-frequency gravity waves (HF-GWs) could actually constitute the coupling process between tropospheric convection and stratospheric turbulence. For this, we estimate the kinetic energy in the 10 min-3 h period range in the same 3 h segments as before. Periods shorter than 10 min are excluded in order to avoid contamination of the estimated energy by balloon oscillations, which peak at periods of 3–4 min (Wilson et al., 2023), as well as by instrumental noise. This intrinsic period range typically corresponds to HF-GWs.

The gravity-wave kinetic energy is estimated using the three components of the wind measured along the balloon flights. As explained in Section 3.1, the horizontal velocities are deduced from GPS position. The vertical velocity of air parcels (w_p) is inferred from the balloon vertical motion assuming a linear response of superpressure balloons to gravity-wave-induced displacements. For intrinsic wave periods longer than about 10 min, the vertical displacement of isentropic air parcels (ζ_p) is linearly related to the balloon displacement (ζ_b) on an isopycnic surface: $\zeta_b = \alpha\zeta_p$, with $\alpha \approx 0.3$ (Vincent and Hertzog, 2014; Podglajen et al., 2014). We therefore estimate air-parcel vertical velocities as $w_p = \frac{w_b}{\alpha}$.

We estimate the power spectral densities (PSD) of the detrended velocity components (u, v, w_p) within each 3 h segment using Welch's method. The HF-GW kinetic energy, denoted E_{GW}, is then obtained by integrating the sum of the corresponding PSDs over the selected frequency band:

$$E_{GW} = \frac{1}{2} \int_{1/3\,\mathrm{h}}^{1/10\,\mathrm{min}} [P_{uu}(f) + P_{vv}(f) + P_{ww}(f)]\,\mathrm{d}f = \frac{1}{2}(u'^2 + v'^2 + w_p'^2) \tag{9}$$

where $P_{uu}(f)$, $P_{vv}(f)$, and $P_{ww}(f)$ are the power spectral densities of the three velocity components.

https://doi.org/10.5194/egusphere-2026-2520
Preprint. Discussion started: 22 May 2026

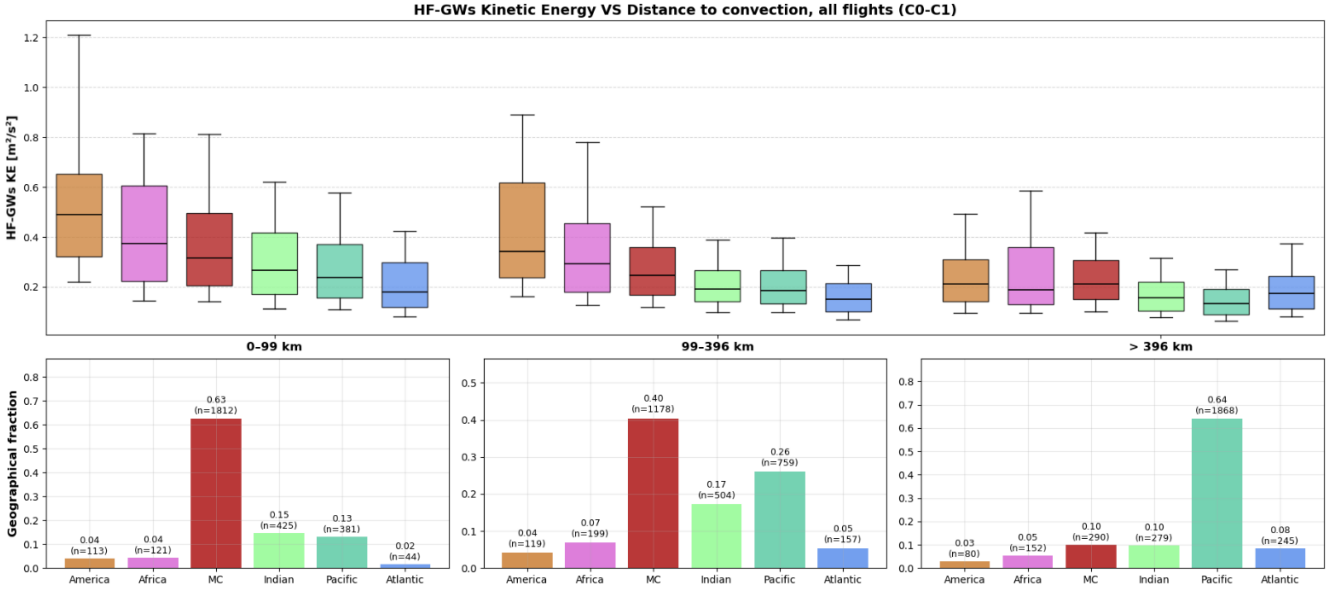

Figure 10. The upper panel shows the HF-GW kinetic energy estimated on 3h-segments (10 min-3 h) per class of distance to convection for each region, all flights of both campaigns. The boxplots represent the 25th and 75th percentiles while whiskers show the 10th and 90th percentiles and black lines, the medians of distributions. The lower panel exhibits the fraction of data in each distance to convection class corresponding to each region.

This quantity provides a measure of high-frequency GW activity, suitable for comparison with turbulence diagnostics and convective proxies.

4.3.2 HF-GW kinetic energy and proximity to deep convection

The top row of Figure 10 displays boxplots of HF-GW kinetic energy computed over 3h segments for all regions, and for three equiprobable bins of distance to convection. As in Figure 9, the second row shows the share of each geographical region in each distance bin.

Figure 10 shows that the HF-GW kinetic energy decreases for all regions as the distance to convection increases, except for the Atlantic ocean where it remains nearly constant. This decrease is strongest over the most active regions (America, Africa and the Maritime Continent), where it can reach up to a factor of 2 for the medians. These results are consistent with those of Corcos et al. (2021), who studied the evolution of GW momentum fluxes with the balloon distance to deep convection. They found a similar decrease of the wave fluxes with increasing distance to convection, and showed that the decrease was stronger for high-frequency-vertically-propagating GWs. Similarly to Corcos et al. (2021), we also find a nearly constant GW energy far away from deep convection, suggesting other potential sources of gravity waves (*e.g.*, shallow convection).

https://doi.org/10.5194/egusphere-2026-2520
Preprint. Discussion started: 22 May 2026

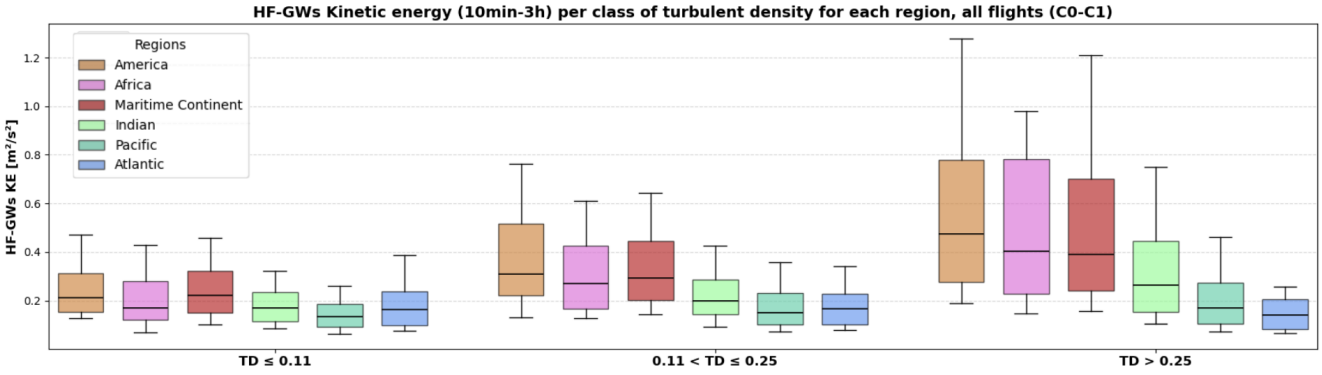

Figure 11. Kinetic energy associated with HF-Gravity waves (10 min-3 h) as a function of turbulence density on 3h-segments, all flights, both campaigns. The boxplots and whiskers represent the 25th-75th and the 10th-90th percentiles respectively, and black lines indicates the medians of distributions.

4.4 HF-GW Kinetic energy and turbulence density

In Figure 11, we display the HF-GW kinetic energy in the same three equiprobable classes of turbulent density than those shown in Figure 9. A marked contrast between continental and oceanic regions can be observed in the HF-GW kinetic energy levels for the higher turbulent density bin, with stronger energy over the continents. Fo the lowest turbulent density class, there is almost no geographical variability in the distributions of HF-GWs energy. Over the continents, Maritime Continent and to some extent the Indian Ocean, the wave energy significantly increases with turbulent density in the 3 h segments. This correlation is observed at the median wave energy, but it is even more pronounced at the 90th energy percentile, strongly suggesting that the largest-amplitude gravity-wave packets are a significant source of turbulence in the lower tropical stratosphere.

As before, the Atlantic Ocean stands out with almost no difference in wave energy with turbulent density, even though we may note that the Atlantic Ocean represents an overall very small share of the balloon dataset. A similar behaviour is found over the Pacific Ocean, which represents nearly one quarter of the data points in the higher turbulence density bin. Hence, while tropical stratospheric turbulence is likely linked to deep convection (*via* gravity waves) over the continents, the Maritime Continent and to some extent the Indian Ocean, other processes may be involved over the Atlantic and Pacific oceans. We investigate some of them in the following section.

5 Larger-scale sources of turbulence

In this section, we focus on the turbulent events detected far away from deep convection (teal and green points in Fig. 8), and particularly those observed over the Pacific ocean. The previous section has shown that these events are unlikely to be primarily

https://doi.org/10.5194/egusphere-2026-2520
Preprint. Discussion started: 22 May 2026

driven by HF-GWs, thus, we now examine larger-scale processes. For this, we use ERA-5 reanalysis on the 50 hPa and 70 hPa levels that roughly correspond to the flight level of STR and TTL balloons respectively. These levels are typically separated by about 2 km in the tropical lower stratosphere. Vertical gradients $X_z^{\text{ERA-5}} = \frac{\Delta X_{\text{ERA-5}}}{\Delta Z_{\text{ERA-5}}}$, where $X_{\text{ERA-5}} = u, v$ or T, are computed between these two levels with the help of the hypsometric equation:

$$\Delta Z_{\text{ERA-5}} = \frac{R_a \langle T \rangle}{g} \ln\left(\frac{P_{70\text{ hPa}}}{P_{50\text{ hPa}}}\right) \tag{10}$$

with $\langle T \rangle$ denotes the averaged temperature between the 50 hPa and 70 hPa levels.

We show in Figure 12 Hovmöller diagrams of these gradients averaged in the $\pm$ 5° latitude band for the time period of the second Strateole-2 campaign (C1). Figure 12 clearly exhibits the signature of eastward-propagating Kelvin waves in T_z^{ERA-5} and u_z^{ERA-5} with periods between 5 and 15 days. The v_z^{ERA-5} Hovmöller diagram, on the other hand, shows signatures of mixed Rossby-gravity waves, for which the wave-packet envelope propagates eastward, but the phase generally propagates westward. The period of those wave-packets is shorter, typically 4-5 days. The symmetric(+)/anti-symmetric(-) decomposition of these signals with respect to the equator (Matsuno, 1966), and the zonal wavenumber (k)/ground-based frequency (ω) spectra (both shown in Appendix B, Fig.B2-B3) further support the above interpretations.

We also note the presence of a meandering feature in both T_z^{ERA-5} and u_z^{ERA-5} diagrams that extends from November 2021 to February 2022 over the central Pacific Ocean (near 200°E). This feature is associated with enhanced negative gradients of u and T. We show in Appendix B, Figure B1, that this pattern results from a dipolar structure in $u'+$ at level 70 hPa indicating a convergence zone: eastward $u'+$ (> 0) at 200-225°E, and westward $u'+$ (< 0) at 225-260°E. Such a convergence induces a subsidence zone (225°E) characterized by a positive signal in $T'+$ due to adiabatic compression. This pattern is even more pronounced at 100 hPa but almost entirely vanishes at 50 hPa (Fig. B1).

As depicted in Figure 13, we interpret this pattern as being associated with both the vertical shear of zonal wind due to the QBO circulation and the upper branch of the Walker circulation, whose strength decreases from the upper troposphere (100 hPa) to the lower stratosphere (50 hPa).

The C1-campaign indeed took place during the end of an eastward QBO phase that was responsible for a negative vertical gradient of zonal-mean wind in the lower stratosphere. Over the Pacific Ocean, the upper-part of the Walker circulation (teal arrows in Fig. 13) is associated with converging eastward winds in the western part of the basin, and westward winds in the eastern part. Hence, the vanishing upper-part of Walker circulation tends to reinforce the negative QBO gradient over the western Pacific Ocean and, on the other hand, to reduce this gradient over the eastern Pacific Ocean. In addition, the converging

https://doi.org/10.5194/egusphere-2026-2520
Preprint. Discussion started: 22 May 2026

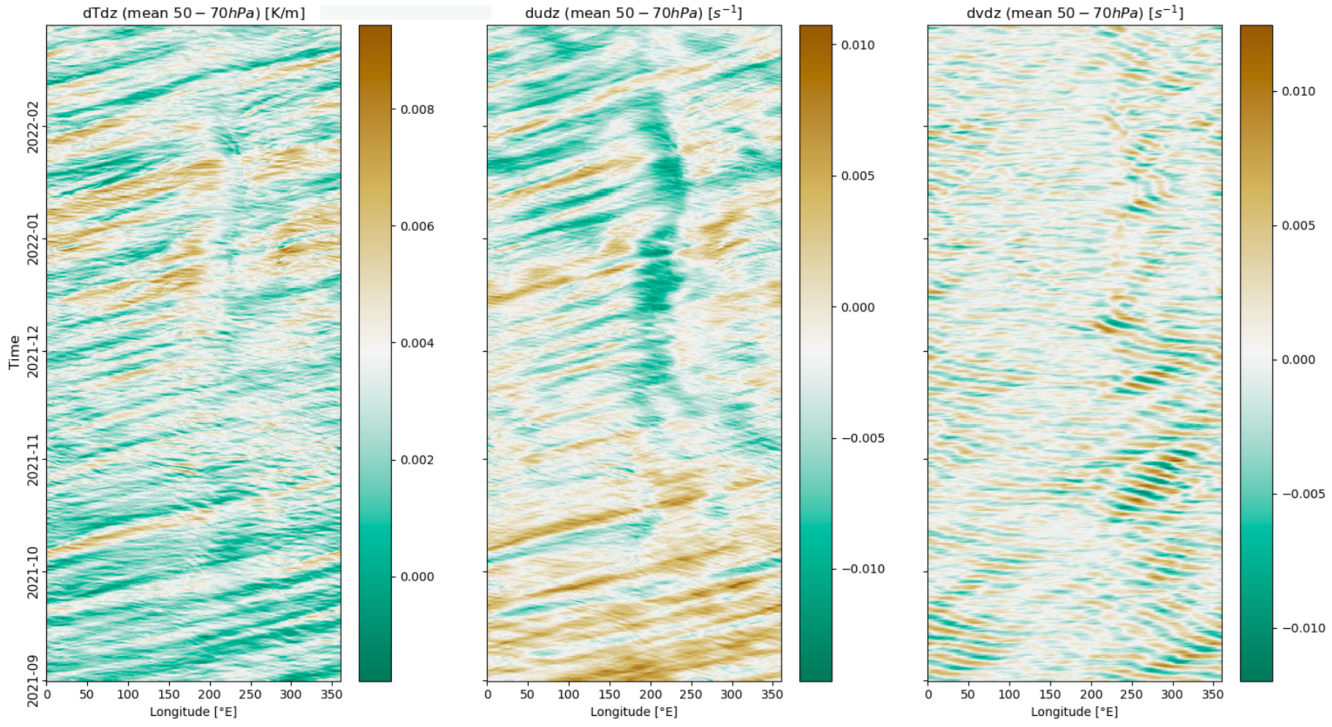

Figure 12. Hovmöller diagrams of large-scale vertical gradients of respectively temperature, zonal wind and meridional wind, computed from ERA-5 fields in the ± 5° latitude band, between 70 hPa and 50 hPa levels, covering the time period of C1-campaign.

Walker winds are associated with a positive temperature anomaly over the central Pacific at 100 and 70 hPa. As this anomaly also vanishes above, it induces a negative temperature gradient (reduced stability), which is observed on the left panel of Figure 12. We also note that a strong La Niña event was active during the boreal winter 2021-2022 (C1-campaign), the sixth strongest since 1982 according to the National Oceanic and Atmospheric Administration (van Oldenborgh et al., 2021; Li et al., 2022). La Niña events are characterized by enhanced deep convection above the Maritime continent and America, which contributes to an increased Walker circulation in the western Pacific Ocean.

https://doi.org/10.5194/egusphere-2026-2520
Preprint. Discussion started: 22 May 2026

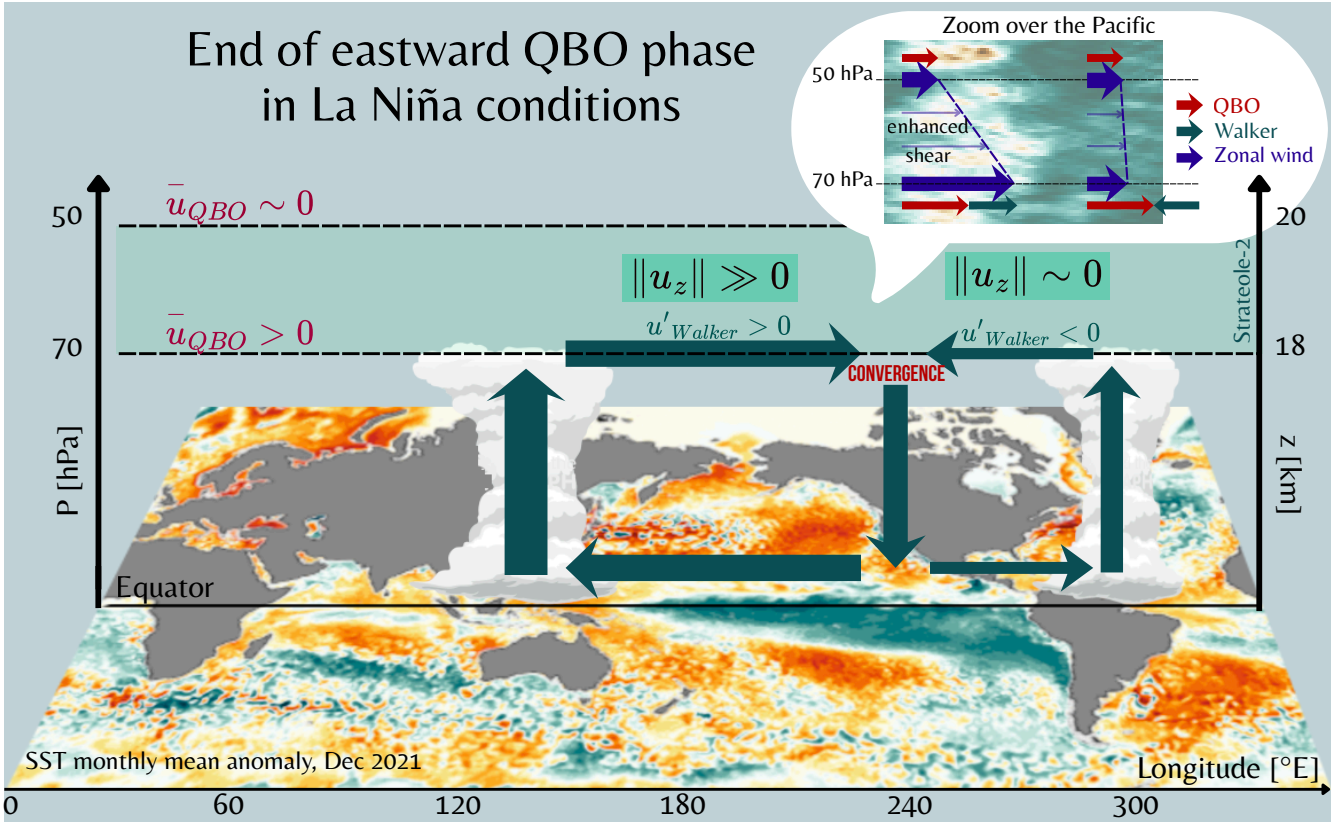

Figure 13. Schematic of the Walker circulation, in the "La Niña" conditions during the C1-campaign. The green layer between 70 and 50 hPa corresponds to the Strateole-2 flight area. The dark red arrows correspond to the zonal background winds associated with the QBO at each level (eastward at 70 hPa, and almost neutral at 50 hPa); the teal ones, to the Walker circulations; and the navy ones represent the mean zonal wind resulting from both the QBO and Walker circulation. The orange and teal areas on the map represent the positive and negative sea surface temperature (SST) anomalies (monthly mean) associated with December 2021.

Figure 14 shows the resulting effect of these large-scale gradients in static stability (${N^2}_{ERA-5}$), shear (S^2_{ERA-5}) and ultimately in the Richardson number (Ri_{ERA-5}), all derived from ERA-5 reanalyses. The enhanced shear and reduced stability combine to produce a large-scale reduced Richardson number pattern over the central Pacific Ocean, with background values close to unity. We furthermore display in Figure 14 the turbulent events detected in the balloon time-series, which took place in the $\pm 5°$ latitude band during the C1-campaign. The color code distinguishes those that are located less than 100 km away from deep convection (red) to those that took place farther away (blue). The non-convective turbulent events appear to cluster within the anomalous low Richardson-number area over the Pacific ocean. These turbulent events were therefore likely favored by the reduced stability produced by the large-scale convergence of the Walker circulation in the upper troposphere and lower stratosphere.

https://doi.org/10.5194/egusphere-2026-2520
Preprint. Discussion started: 22 May 2026

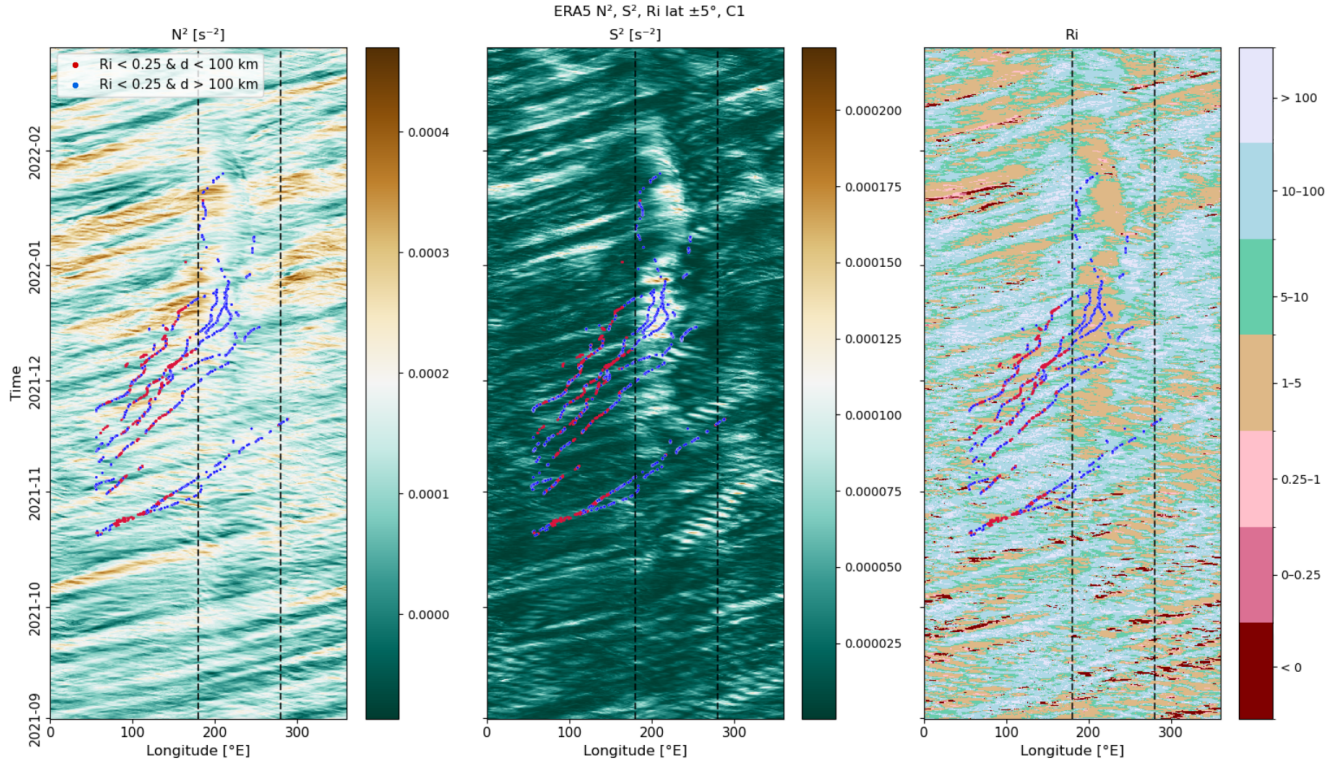

Figure 14. Hovmöller diagrams of large-scale Brunt-Väisälä Frequency (N^2), squared shear (S^2) and gradient Richardson number (Ri), computed from ERA-5 fields in the +/-5° latitude band, between 70 hPa and 50 hPa levels, covering the time period of C1-campaign. The colored dots represent turbulent events detected along the flight paths of the balloons, closer than 100 km to deep convection (red) and farther (blue), within the same latitude band during C1-campaign. The black dashed lines correspond to the boundaries of the Pacific region.

The Strateole-2 dataset that encompasses only two years does not allow us to further investigate the role of the Walker circulation on the occurrence of turbulence in the lower stratosphere. We nevertheless note that the location and strength of the low Richardson-number area is very likely modulated by the QBO phases, as well as by the intensity of the El Niño/La Niña events.

425 In addition, although we do not detect clear signatures of the effect of stratospheric planetary waves in turbulence occurrences in the Strateole-2 dataset, Figure 14 suggests that such conditions may occur. The right panel of this figure for instance clearly exhibits patches of very low Richardson numbers associated with the propagation of Kelvin waves from September 2021 to November 2022. Similar signatures were not obvious in the time and location sampled by the Strateole-2 balloons, and the large-scale low Richardson numbers were dominated by the meandering feature described above.

https://doi.org/10.5194/egusphere-2026-2520
Preprint. Discussion started: 22 May 2026

6 Conclusions

In this paper, the frequency of turbulence events in the tropical lower stratosphere is estimated from Strateole-2 *in situ* long-duration balloon observations. In particular, the vertical oscillations of superpressure balloons about their equilibrium level are used to infer vertical gradients of winds and temperature along the balloon trajectories, from which local estimates of the Richardson number are derived. These estimates are typically obtained at a space and time resolution of a few tens of meters and 110 s.

Based on a classical Richardson number criterion ($Ri < 0.25$), these Lagrangian Ri time series reveal a mean turbulent fraction of 0.178 in nighttime data (0.225 in daytime data) in the tropics during the 2019 and 2021 boreal winters. This fraction is typically one order of magnitude larger than previously reported values for similar latitudes and QBO conditions (Atlas et al., 2025). Yet, our estimates are obtained at significantly finer vertical scales than those in Atlas et al. (2025), who analyzed radiosoundings with vertical resolutions exceeding 200 m, highlighting a strong scale dependence of inferred turbulence statistics.

Geographical differences in turbulent fractions are investigated and reveal a clear contrast between continental and oceanic regions, with systematically larger values over the continents and the Maritime Continent. The analysis of turbulent event density on 3 h flight segments shows that higher turbulent densities are systematically associated with shorter balloon distances to deep convection. In agreement with Corcos et al. (2021), we also find enhanced activity of short-period (10 min-3 h) gravity waves near deep convective systems, thereby supporting the major role of deep convection in generating gravity waves in the tropics. Finally, we also observe a clear link between densities of turbulent events and short-period gravity-wave activity, for all regions except the Atlantic Ocean (where the turbulent fraction remains low, 0.12) and the eastern Pacific Ocean. This relationship therefore suggests that a significant fraction of turbulence occurrences in the tropical lower stratosphere may result from the breaking of convectively generated gravity waves.

Over the central Pacific Ocean, we identify an area of increased wind shear and reduced stability resulting from the modulation of the zonal-mean QBO shear by the vanishing Walker circulation in the tropical lower stratosphere. This feature is likely enhanced by the La Niña phase of ENSO that took place during the 2021-2022 Strateole-2 campaign. A major fraction of turbulence occurrences observed over the Pacific Ocean clusters in this low Richardson number area, suggesting that large-scale circulations can also create favorable conditions for the appearance of turbulence in the tropical lower stratosphere.

Overall, our results highlight the multiscale nature of turbulence generation in the tropical lower stratosphere. Turbulent events appear to result from interactions between processes spanning a wide range of spatial and temporal scales, from deep convection and high-frequency gravity waves to planetary-scale circulations such as the QBO and Walker circulation, rather

https://doi.org/10.5194/egusphere-2026-2520
Preprint. Discussion started: 22 May 2026

than being solely controlled by resolved-scale stability and shear conditions. This multiscale coupling likely contributes to the strong intermittency and spatial heterogeneity of turbulence in the TTL, consistent with previous radar and balloon observations (Alisse and Sidi, 2000; Wilson et al., 2012; Luce et al., 2014). Such intermittency is difficult to represent in models relying on quasi-continuous diffusive mixing formulations or on diagnostics based solely on resolved-scale stability conditions. Because turbulence occurrence appears to emerge from multiscale interactions, representing these processes may require parameterizations that better account for intermittency and gravity-wave-driven mixing (Fritts and Alexander, 2003; Alexander et al., 2010; Geller et al., 2013).

These findings also have implications for the representation of mixing and momentum deposition in current general circulation models (GCMs) and reanalyses. The turbulence events identified in the Strateole-2 observations occur at vertical scales of a few tens of meters, far below the effective resolution of current global models and reanalysis products. In particular, many turbulent events detected from the high-resolution balloon observations are associated with only moderate large-scale Richardson numbers in ERA-5 ($Ri_{ERA-5} \sim O(1)$), suggesting that large-scale fields may capture environments favorable to turbulence generation while failing to resolve the small-scale instabilities and wave-breaking processes that ultimately trigger turbulence. This result is also consistent with previous studies showing that Richardson-number estimates strongly depend on the vertical scale over which they are computed (Balsley et al., 2008), and that thin turbulent layers can exist even when the background flow appears stable at larger scales (Haack et al., 2014).

Improving the representation of such small-scale turbulent mixing is important because it may affect tracer transport and dehydration processes in the TTL, including the distribution of water vapour and ozone and the exchange between the troposphere and the stratosphere (Fueglistaler et al., 2009; Podglajen et al., 2017).

This study has two main limitations. First, as we have shown above, instrumental noise, primarily noise in the temperature data, prevents us from estimating the gradient Richardson number Ri when the amplitude of the balloon's oscillations is small. We must therefore exclude approximately half of the data from the Ri time series. Second, as things stand, the Strateole-2 flight dataset does not allow us to estimate the intensity of turbulent events, which in turn prevents us from estimating turbulence energy or mixing properties. The first limitation is intrinsic to the current instrumental configuration. Regarding the second one, the Strateole-2 flights in the next campaign (C2), scheduled for October 2026, will carry a high-frequency anemometer (0.2 to 1 Hz) capable of measuring relative vertical wind of the air. We thus hope to be able to detect and quantify turbulence directly from these wind measurements during the flights.

https://doi.org/10.5194/egusphere-2026-2520
Preprint. Discussion started: 22 May 2026

Furthermore, the next campaign will correspond to a different phase of QBO (westward winds). These data, combined with complementary observations, will also help investigate the seasonal and interannual variability of turbulence occurrence in the tropical lower stratosphere, as well as its sensitivity to QBO and ENSO phases.

Data availability. The balloon-borne TSEN data were collected as part of Strateole-2, which is sponsored by CNES, CNRS/INSU, NSF, and ESA. Strateole-2 TSEN data are available at https://data.ipsl.fr/catalog/strateole2/ and https://thredds-x.ipsl.fr/thredds/catalog/C1/catalog.html.

The merged IR satellite images were obtained from the NOAA/NCEP GPM_MERGIR_1 product, available at https://disc.gsfc.nasa.gov/datasets/GPM_MERGIR_1/summary.

The ERA5 reanalysis data are available at https://apps.ecmwf.int/data-catalogues/era5/?type=an&class=ea&stream=oper&expver=1.

Appendix A

A1 Uncertainties estimates

We can write an estimate of the uncertainty on our $|Ri|$ estimates as follow, considering uncertainties on potential temperature, horizontal winds and vertical displacement amplitudes.

$$Ri = \frac{N^2}{S^2} \rightarrow \frac{\delta Ri}{Ri} = \sqrt{\left(\frac{\delta N^2}{N^2}\right)^2 + \left(\frac{\delta S^2}{S^2}\right)^2} \tag{A1}$$

with $\frac{\delta X}{X}$ meaning the relative uncertainty on X.

$$N^2 = \frac{g}{\bar{\theta}}\frac{\Delta\bar{\theta}}{\Delta z} \rightarrow \frac{\delta N^2}{N^2} = \sqrt{\left(\frac{\delta\Delta\bar{\theta}}{\Delta\bar{\theta}}\right)^2 + \left(\frac{\delta\Delta z}{\Delta z}\right)^2} \tag{A2}$$

with ΔX meaning the differences estimated with the "envelope method" (between successive extrema).

$$S^2 = \left(\frac{\Delta u}{\Delta z}\right)^2 + \left(\frac{\Delta v}{\Delta z}\right)^2 \rightarrow \delta S^2 = \sqrt{\left[\delta\left(\frac{\Delta u}{\Delta z}\right)^2\right]^2 + \left[\delta\left(\frac{\Delta v}{\Delta z}\right)^2\right]^2} \tag{A3}$$

https://doi.org/10.5194/egusphere-2026-2520
Preprint. Discussion started: 22 May 2026

$$\frac{\delta\left(\frac{\Delta u}{\Delta z}\right)^2}{\left(\frac{\Delta u}{\Delta z}\right)^2} = 2 \cdot \frac{\delta\left(\frac{\Delta u}{\Delta z}\right)}{\left(\frac{\Delta u}{\Delta z}\right)} = 2\sqrt{\left(\frac{\delta\Delta u}{\Delta u}\right)^2 + \left(\frac{\delta\Delta z}{\Delta z}\right)^2} \tag{A4}$$

$$\delta S^2 = 2\sqrt{\left(\frac{\Delta u}{\Delta z}\right)^4 \cdot \left[\left(\frac{\delta\Delta u}{\Delta u}\right)^2 + \left(\frac{\delta\Delta z}{\Delta z}\right)^2\right] + \left(\frac{\Delta v}{\Delta z}\right)^4 \cdot \left[\left(\frac{\delta\Delta v}{\Delta v}\right)^2 + \left(\frac{\delta\Delta z}{\Delta z}\right)^2\right]} \tag{A5}$$

$$\frac{\delta S^2}{S^2} = 2\frac{\sqrt{\left(\frac{\Delta u}{\Delta z}\right)^4 \cdot \left[\left(\frac{\delta\Delta u}{\Delta u}\right)^2 + \left(\frac{\delta\Delta z}{\Delta z}\right)^2\right] + \left(\frac{\Delta v}{\Delta z}\right)^4 \cdot \left[\left(\frac{\delta\Delta v}{\Delta v}\right)^2 + \left(\frac{\delta\Delta z}{\Delta z}\right)^2\right]}}{\left(\frac{\Delta u}{\Delta z}\right)^2 + \left(\frac{\Delta v}{\Delta z}\right)^2} \tag{A6}$$

$$\frac{\delta S^2}{S^2} \approx 2\sqrt{\left(\frac{\delta\Delta u}{\Delta u}\right)^2 + \left(\frac{\delta\Delta v}{\Delta v}\right)^2 + 2\left(\frac{\delta\Delta z}{\Delta z}\right)^2} \tag{A7}$$

We deduce the following approximation for the relative uncertainty on Ri :

$$\frac{\delta Ri}{Ri} \approx \sqrt{\left(\frac{\delta\Delta\theta}{\Delta\theta}\right)^2 + \left(\frac{\delta\Delta z}{\Delta z}\right)^2 + 4\left[\left(\frac{\delta\Delta u}{\Delta u}\right)^2 + \left(\frac{\delta\Delta v}{\Delta v}\right)^2 + 2\left(\frac{\delta\Delta z}{\Delta z}\right)^2\right]} \tag{A8}$$

$$\frac{\delta Ri}{Ri} \approx \sqrt{\left(\frac{\delta\Delta\theta}{\Delta\theta}\right)^2 + 4\left(\frac{\delta\Delta u}{\Delta u}\right)^2 + 4\left(\frac{\delta\Delta v}{\Delta v}\right)^2 + 9\left(\frac{\delta\Delta z}{\Delta z}\right)^2} \tag{A9}$$

If we consider $\delta\Delta\theta = \sqrt{2}\sigma_\theta$; $\delta\Delta u \approx \delta\Delta v = \sqrt{2}\sigma_{u,v}$; $\delta\Delta z = \sqrt{2}\sigma_z$ and $\Delta\theta = \frac{\bar{\theta}}{g}N^2\Delta z$ and $\Delta u \approx \Delta v \approx \frac{S}{\sqrt{2}}\Delta z$, we can rewrite the relative uncertainty on Ri as:

$$\frac{\sigma_{Ri}}{Ri} \approx \frac{1}{|\Delta z|}\sqrt{2(\sigma_\theta)^2 \cdot \left(\frac{\beta_\theta}{N^2}\right)^2 + 18(\sigma_z)^2 + 16\frac{(\sigma_{u,v})^2}{S^2}} \tag{A10}$$

https://doi.org/10.5194/egusphere-2026-2520
Preprint. Discussion started: 22 May 2026

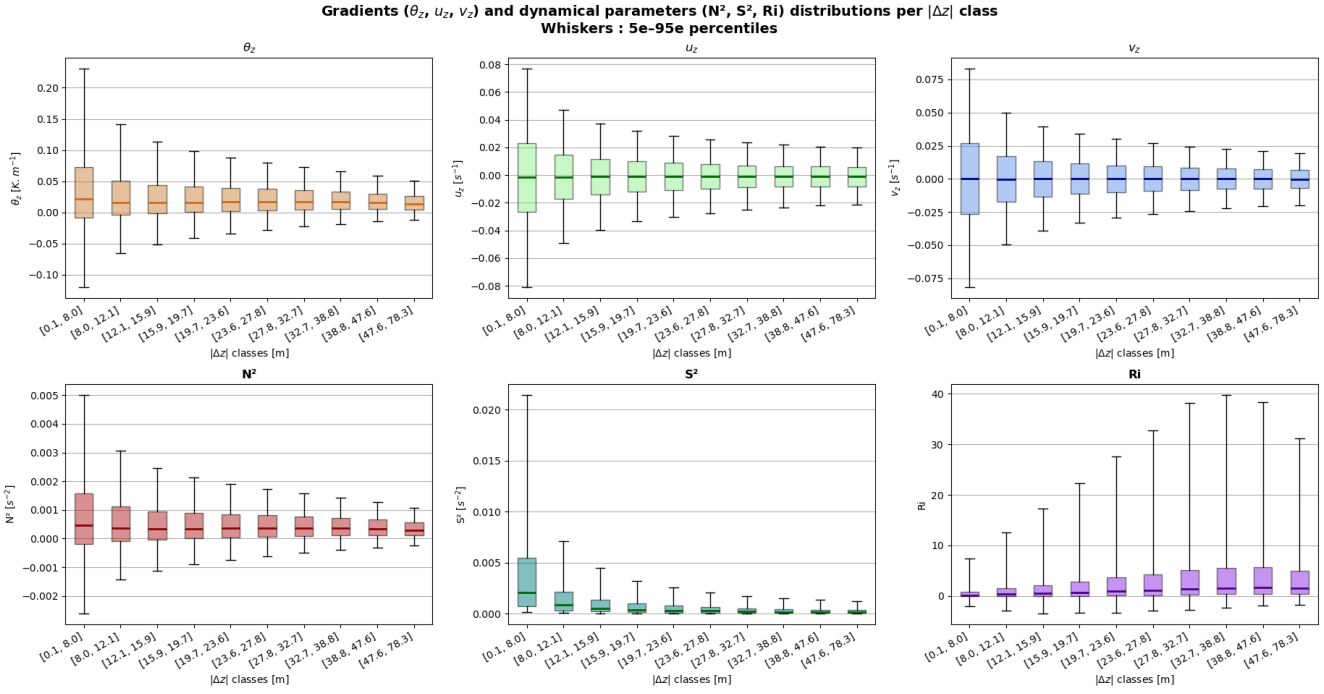

Figure A1. Distributions of vertical gradients θ_z, u_z, v_z (first raw), N^2, S^2 and Ri estimates (second raw) for equiprobable bins of balloon-vertical-oscillation amplitudes, both campaigns.

Figure A1 shows the distributions of the vertical gradient estimates θ_z (orange), u_z (light green), v_z (blue) and corresponding N^2 (red), S^2 (green) and Ri (purple) for equiprobable classes of $|\Delta z|$ during both campaigns. The horizontal lines represent the medians and the boxes and whiskers correspond to the 25th-75th and 5th-95th percentiles, respectively. We can notice that the dispersion of gradients, N^2 and S^2 values is much more important for small $|\Delta z|$ classes, and decreases as $|\Delta z|$ increases. To avoid the effect on the estimation of the Ri relative uncertainty, we chose to use averaged values of N^2 and S^2 in the previous equation A10.

Appendix B: ERA-5

B1 Hovmöller diagrams

In order to characterize the large-scale wave activity, we plot Hovmöller diagrams of winds and temperature, each field is taken in the latitude band of 5°. We remove a zonal mean for each time to obtain the anomalies. Then, we separate each field in a symmetric ("+") and an antisymmetric ("-") part with respect to the equator, to better see the contribution of each type of wave, using the theory developed by Matsuno (1966) :

https://doi.org/10.5194/egusphere-2026-2520
Preprint. Discussion started: 22 May 2026

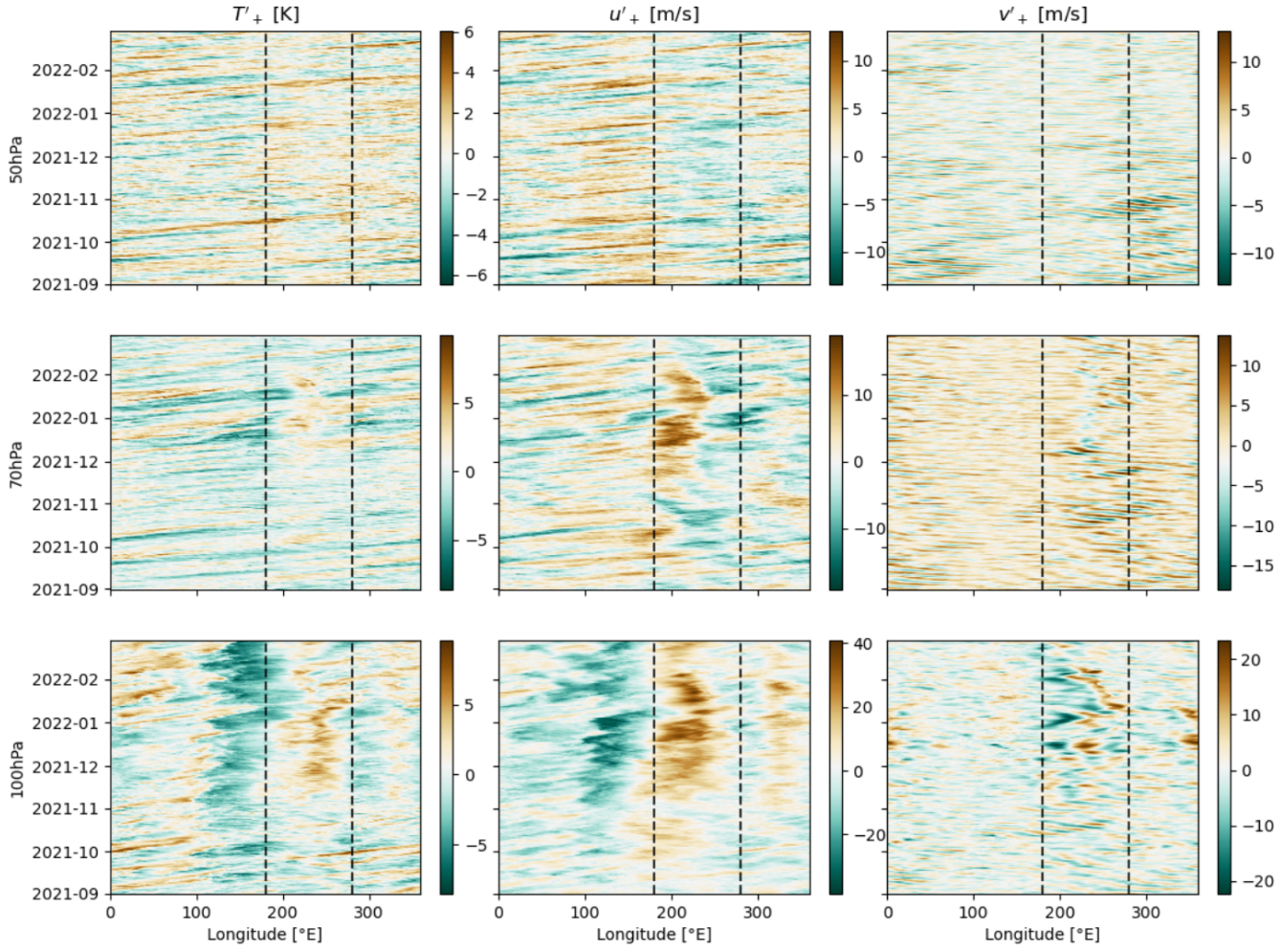

Figure B1. Hovmöller diagrams of temperature, zonal wind and meridional wind symmetrical anomalies with respect to the equator in the latitude band +/-5° during C1-campagain, from ERA5 fields at 50 (up), 70 (middle) and 100 hPa (down). The black dashed lines correspond to the boundaries of the Pacific region.

- Kelvin waves : signatures in $u'+$ and $T'+$
- Mixed Rossby Gravity waves : signatures in $v'+$, $T'-$ and $u'-$
- Equatorial Rossby waves : signature in $u'+$, $T'+$ and $v'-$
- Inertia Gravity waves : everywhere

https://doi.org/10.5194/egusphere-2026-2520
Preprint. Discussion started: 22 May 2026

B2 $k - \omega$ spectra

With a 2D Fourier transform in time and longitude, we compute $k - \omega$ spectra for each symmetric and antisymmetric anomaly field. With the dispersion relations for each wave, we deduce equivalent heights (he) that correspond to the limits of the spectral domain filled by each wave. We can then isolate the greater modes of each wave and plot the corresponding Hovmöller diagrams.

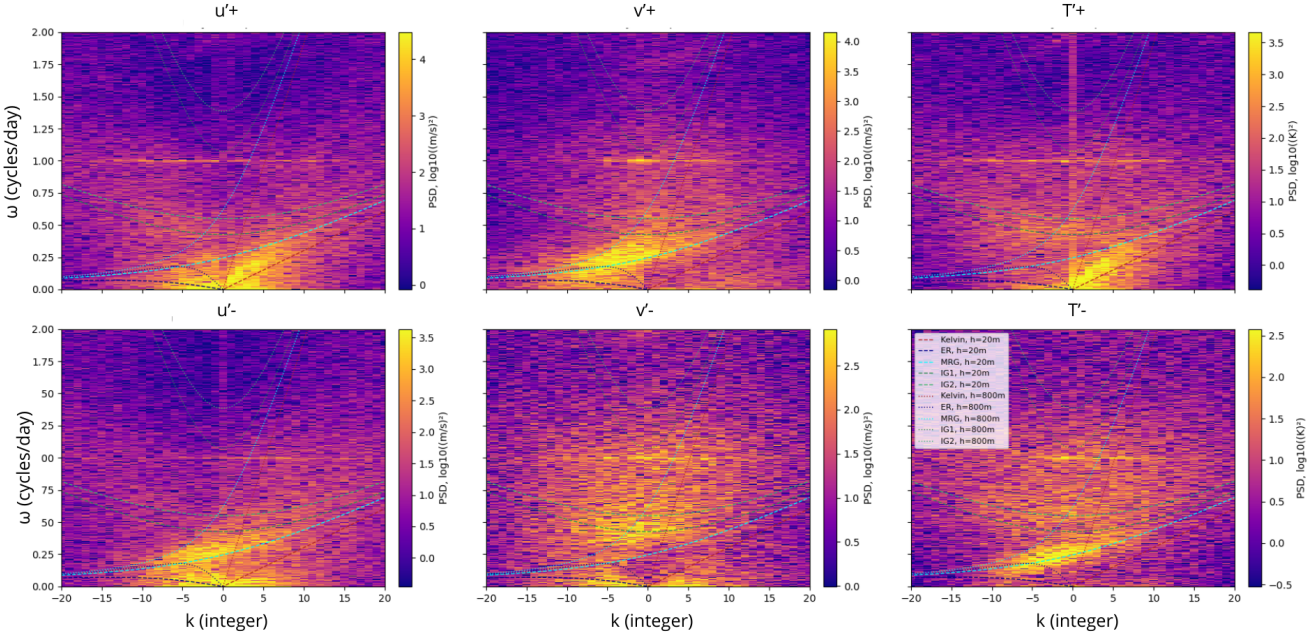

Figure B2. $k - \omega$ spectra for symmetric (+) and antisymmetric (-) zonal wind, meridional wind and temperature anomalies with respect to the equator, at 70 hPa, during C1-campaign, from ERA-5 fields.

https://doi.org/10.5194/egusphere-2026-2520
Preprint. Discussion started: 22 May 2026

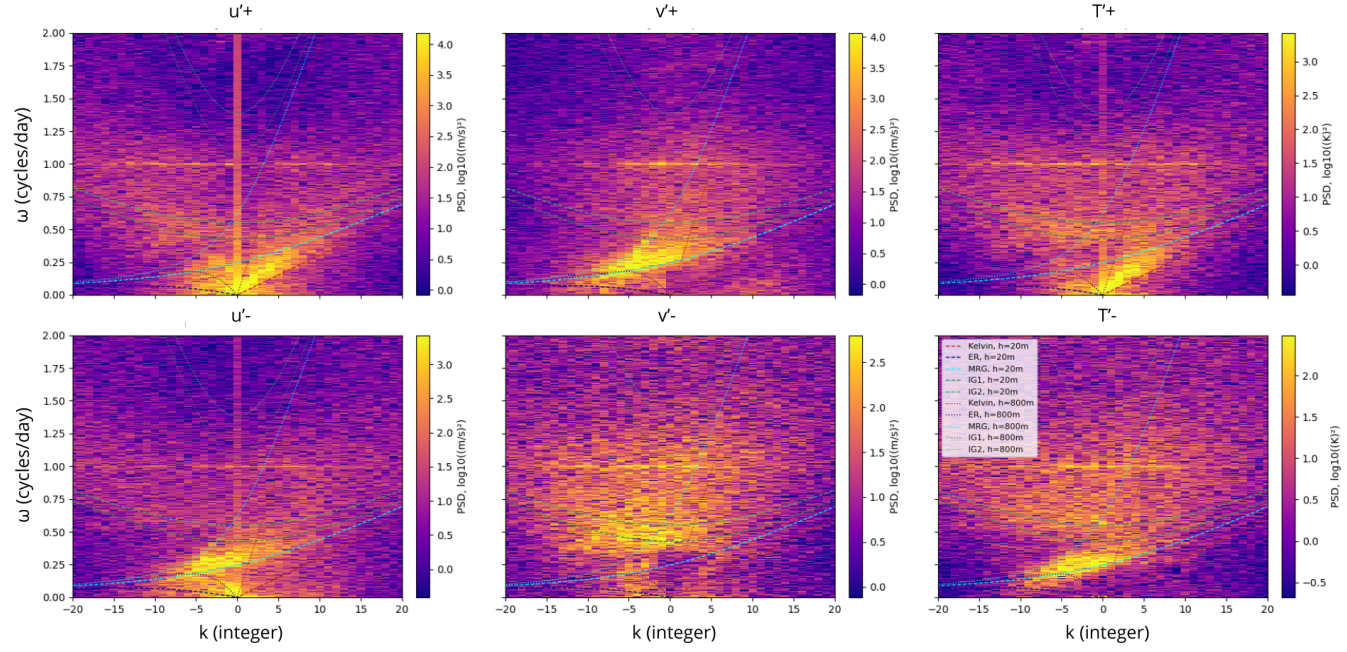

Figure B3. $k - \omega$ spectra for symmetric (+) and antisymmetric (-) zonal wind, meridional wind and temperature anomalies with respect to the equator, at 50 hPa, during C1-campaign, from ERA-5 fields.

Author contributions. F.J designed the study, processed the Strateole-2 observations, and performed the turbulence analysis. F.J. developed the methodology to estimate the Richardson number and turbulent events, analysed the results and drafted the manuscript.

R.W. and A.H. contributed to the interpretation of the results and to the discussion, providing expertise on turbulence, gravity waves and large-scale dynamics.

All authors contributed to the manuscript revision and approved the final version.

Competing interests. The authors declare no conflicts of interest relevant to this study.

https://doi.org/10.5194/egusphere-2026-2520
Preprint. Discussion started: 22 May 2026

References

Achatz, U.: On the role of optimal perturbations in the instability of monochromatic gravity waves, Physics of Fluids, 17, 094 107, https://doi.org/10.1063/1.2046709, 2005.

Alexander, M. J., Geller, M., McLandress, C., Polavarapu, S., Preusse, P., Sassi, F., Sato, K., Eckermann, S., Ern, M., Hertzog, A., Kawatani, Y., Pulido, M., Shaw, T. A., Sigmond, M., Vincent, R., and Watanabe, S.: Recent developments in gravity-wave effects in climate models and the global distribution of gravity-wave momentum flux from observations and models, Quarterly Journal of the Royal Meteorological Society, 136, 1103–1124, https://doi.org/10.1002/qj.637, _eprint: https://rmets.onlinelibrary.wiley.com/doi/pdf/10.1002/qj.637, 2010.

Alisse, J.-R. and Sidi, C.: Experimental probability density functions of small-scale fluctuations in the stably stratified atmosphere, Journal of Fluid Mechanics, 402, 137–162, https://doi.org/10.1017/S0022112099006813, 2000.

Alisse, J.-R., Haynes, P. H., Vanneste, J., and Sidi, C.: Quantification of stratospheric mixing from turbulence microstructure measurements, Geophysical Research Letters, 27, 2621–2624, https://doi.org/10.1029/2000GL011386, _eprint: https://agupubs.onlinelibrary.wiley.com/doi/pdf/10.1029/2000GL011386, 2000.

Andrews, D. G., Leovy, C. B., and Holton, J. R.: Middle Atmosphere Dynamics, Academic Press, ISBN 978-0-08-051167-2, google-Books-ID: hpZiDwAAQBAJ, 1987.

Atlas, R. and Bretherton, C. S.: Aircraft observations of gravity wave activity and turbulence in the tropical tropopause layer: prevalence, influence on cirrus clouds, and comparison with global storm-resolving models, Atmospheric Chemistry and Physics, 23, 4009–4030, https://doi.org/10.5194/acp-23-4009-2023, 2023.

Atlas, R., Podglajen, A., Wilson, R., Hertzog, A., and Plougonven, R.: Turbulence in the tropical stratosphere, equatorial Kelvin waves, and the quasi-biennial oscillation, Proceedings of the National Academy of Sciences, 122, e2409791 122, https://doi.org/10.1073/pnas.2409791122, 2025.

Baldwin, M. P., Gray, L. J., Dunkerton, T. J., Hamilton, K., Haynes, P. H., Randel, W. J., Holton, J. R., Alexander, M. J., Hirota, I., Horinouchi, T., Jones, D. B. A., Kinnersley, J. S., Marquardt, C., Sato, K., and Takahashi, M.: The quasi-biennial oscillation, Reviews of Geophysics, 39, 179–229, https://doi.org/10.1029/1999RG000073, _eprint: https://agupubs.onlinelibrary.wiley.com/doi/pdf/10.1029/1999RG000073, 2001.

Balsley, B. B., Svensson, G., and Tjernström, M.: On the Scale-dependence of the Gradient Richardson Number in the Residual Layer, Boundary-Layer Meteorol, 127, 57–72, https://doi.org/10.1007/s10546-007-9251-0, 2008.

Brewer, A. W.: Evidence for a world circulation provided by the measurements of helium and water vapour distribution in the stratosphere, Quarterly Journal of the Royal Meteorological Society, 75, 351–363, https://doi.org/10.1002/qj.49707532603, _eprint: https://rmets.onlinelibrary.wiley.com/doi/pdf/10.1002/qj.49707532603, 1949.

Butchart, N.: The Brewer-Dobson circulation, Reviews of Geophysics, 52, 157–184, https://doi.org/10.1002/2013RG000448, _eprint: https://agupubs.onlinelibrary.wiley.com/doi/pdf/10.1002/2013RG000448, 2014.

https://doi.org/10.5194/egusphere-2026-2520
Preprint. Discussion started: 22 May 2026

Corcos, M., Hertzog, A., Plougonven, R., and Podglajen, A.: Observation of Gravity Waves at the Tropical Tropopause Using Superpressure Balloons, Journal of Geophysical Research: Atmospheres, 126, e2021JD035 165, https://doi.org/10.1029/2021JD035165, _eprint: https://agupubs.onlinelibrary.wiley.com/doi/pdf/10.1029/2021JD035165, 2021.

Corcos, M., Bramberger, M., Alexander, M. J., Hertzog, A., Liu, C., and Wright, C.: Observation of Gravity Waves Generated by Convection and the "Moving Mountain" Mechanism During Stratéole-2 Campaigns and Their Impact on the QBO, Journal of Geophysical Research: Atmospheres, 130, e2024JD041 804, https://doi.org/10.1029/2024JD041804, _eprint: https://agupubs.onlinelibrary.wiley.com/doi/pdf/10.1029/2024JD041804, 2025.

Dewan, E. M.: Turbulent Vertical Transport due to Thin Intermittent Mixing Layers in the Stratosphere and Other Stable Fluids, Science, 211, 1041–1042, https://doi.org/10.1126/science.211.4486.1041, 1981.

Dörnbrack, A.: Turbulent mixing by breaking gravity waves, Journal of Fluid Mechanics, 375, 113–141, https://doi.org/10.1017/S0022112098002833, 1998.

Flannaghan, T. J. and Fueglistaler, S.: Kelvin waves and shear-flow turbulent mixing in the TTL in (re-)analysis data, Geophysical Research Letters, 38, https://doi.org/10.1029/2010GL045524, _eprint: https://agupubs.onlinelibrary.wiley.com/doi/pdf/10.1029/2010GL045524, 2011.

Fritts, D. C. and Alexander, M. J.: Gravity wave dynamics and effects in the middle atmosphere, Reviews of Geophysics, 41, https://doi.org/10.1029/2001RG000106, _eprint: https://agupubs.onlinelibrary.wiley.com/doi/pdf/10.1029/2001RG000106, 2003.

Fueglistaler, S., Dessler, A. E., Dunkerton, T. J., Folkins, I., Fu, Q., and Mote, P. W.: Tropical tropopause layer, Reviews of Geophysics, 47, https://doi.org/10.1029/2008RG000267, _eprint: https://agupubs.onlinelibrary.wiley.com/doi/pdf/10.1029/2008RG000267, 2009.

Fujiwara, M., Yamamoto, M. K., Hashiguchi, H., Horinouchi, T., and Fukao, S.: Turbulence at the tropopause due to breaking Kelvin waves observed by the Equatorial Atmosphere Radar, Geophysical Research Letters, 30, https://doi.org/10.1029/2002GL016278, _eprint: https://agupubs.onlinelibrary.wiley.com/doi/pdf/10.1029/2002GL016278, 2003.

Galperin, B., Sukoriansky, S., and Anderson, P. S.: On the critical Richardson number in stably stratified turbulence, Atmospheric Science Letters, 8, 65–69, https://doi.org/10.1002/asl.153, _eprint: https://rmets.onlinelibrary.wiley.com/doi/pdf/10.1002/asl.153, 2007.

Geller, M. A., Alexander, M. J., Love, P. T., Bacmeister, J., Ern, M., Hertzog, A., Manzini, E., Preusse, P., Sato, K., Scaife, A. A., and Zhou, T.: A Comparison between Gravity Wave Momentum Fluxes in Observations and Climate Models, Journal of Climate, 26, 6383–6405, https://doi.org/10.1175/JCLI-D-12-00545.1, 2013.

Glanville, A. A. and Birner, T.: Role of vertical and horizontal mixing in the tape recorder signal near the tropical tropopause, Atmos. Chem. Phys., 17, 4337–4353, https://doi.org/10.5194/acp-17-4337-2017, 2017.

Haack, A., Gerding, M., and Lübken, F.-J.: Characteristics of stratospheric turbulent layers measured by LITOS and their relation to the Richardson number, Journal of Geophysical Research: Atmospheres, 119, 10,605–10,618, https://doi.org/10.1002/2013JD021008, _eprint: https://agupubs.onlinelibrary.wiley.com/doi/pdf/10.1002/2013JD021008, 2014.

https://doi.org/10.5194/egusphere-2026-2520
Preprint. Discussion started: 22 May 2026

Hersbach, H., Bell, B., Berrisford, P., Hirahara, S., Horányi, A., Muñoz-Sabater, J., Nicolas, J., Peubey, C., Radu, R., Schepers, D., Simmons, A., Soci, C., Abdalla, S., Abellan, X., Balsamo, G., Bechtold, P., Biavati, G., Bidlot, J., Bonavita, M., De Chiara, G., Dahlgren, P., Dee, D., Diamantakis, M., Dragani, R., Flemming, J., Forbes, R., Fuentes, M., Geer, A., Haimberger, L., Healy, S., Hogan, R. J., Hólm, E., Janisková, M., Keeley, S., Laloyaux, P., Lopez, P., Lupu, C., Radnoti, G., de Rosnay, P., Rozum, I., Vamborg, F., Villaume, S., and Thépaut, J.-N.: The ERA5 global reanalysis, Quarterly Journal of the Royal Meteorological Society, 146, 1999–2049, https://doi.org/10.1002/qj.3803, _eprint: https://rmets.onlinelibrary.wiley.com/doi/pdf/10.1002/qj.3803, 2020.

Hertzog, A., Cocquerez, P., Guilbon, R., Valdivia, J.-N., Venel, S., Basdevant, C., Boccara, G., Bordereau, J., Brioit, B., Vial, F., Cardonne, A., Ravissot, A., and Schmitt, : Stratéole/Vorcore—Long-duration, Superpressure Balloons to Study the Antarctic Lowe r Stratosphere during the 2005 Winter, Journal of Atmospheric and Oceanic Technology, 24, 2048–2061, https://doi.org/10.1175/2007JTECHA948.1, 2007.

Hines, C. O.: Generation of Turbulence by Atmospheric Gravity Waves, Journal of the Atmospheric Sciences, 45, 1269–1278, https://doi.org/10.1175/1520-0469(1988)045<1269:GOTBAG>2.0.CO;2, 1988.

Howard, L. N.: Note on a paper of John W. Miles, Journal of Fluid Mechanics, 10, 509–512, https://doi.org/10.1017/S0022112061000317, 1961.

Janowiak, J., Joyce, B., and Xie, P.: NCEP/CPC L3 Half Hourly 4km Global (60S - 60N) Merged IR V1, NASA Goddard Earth Sciences Data and Information Services Center (DAAC) data set, p. P4HZB9N27EKU, https://doi.org/10.5067/P4HZB9N27EKU, aDS Bibcode: 2017gdsc.data..253J, 2017.

Jensen, E. J., Ueyama, R., Pfister, L., Bui, T. V., Alexander, M. J., Podglajen, A., Hertzog, A., Woods, S., Lawson, R. P., Kim, J.-E., and Schoeberl, M. R.: High-frequency gravity waves and homogeneous ice nucleation in tropical tropopause layer cirrus, Geophysical Research Letters, 43, 6629–6635, https://doi.org/10.1002/2016GL069426, _eprint: https://agupubs.onlinelibrary.wiley.com/doi/pdf/10.1002/2016GL069426, 2016.

Li, X., Hu, Z.-Z., Tseng, Y.-h., Liu, Y., and Liang, P.: A Historical Perspective of the La Niña Event in 2020/2021, Journal of Geophysical Research: Atmospheres, 127, e2021JD035 546, https://onlinelibrary.wiley.com/doi/abs/10.1029/2021JD035546, 2022.

Lu, B. and Ren, H.-L.: What Caused the Extreme Indian Ocean Dipole Event in 2019?, Geophysical Research Letters, 47, e2020GL087 768, https://doi.org/10.1029/2020GL087768, _eprint: https://agupubs.onlinelibrary.wiley.com/doi/pdf/10.1029/2020GL087768, 2020.

Luce, H., Wilson, R., Dalaudier, F., Hashiguchi, H., Nishi, N., Shibagaki, Y., and Nakajo, T.: Simultaneous observations of tropospheric turbulence from radiosondes using Thorpe analysis and the VHF MU radar, Radio Science, 49, 1106–1123, https://doi.org/10.1002/2013RS005355, 2014.

Matsuno, T.: Quasi-Geostrophic Motions in the Equatorial Area, Journal of the Meteorological Society of Japan. Ser. II, 44, 25–43, https://doi.org/10.2151/jmsj1965.44.1_25, 1966.

https://doi.org/10.5194/egusphere-2026-2520
Preprint. Discussion started: 22 May 2026

Mauritsen, T., Svensson, G., Zilitinkevich, S. S., Esau, I., Enger, L., and Grisogono, B.: A Total Turbulent Energy Closure Model for Neutrally and Stably Stratified Atmospheric Boundary Layers, Journal of the Atmospheric Sciences, 64, 4113–4126, https://doi.org/10.1175/2007JAS2294.1, 2007.

Mega, T., Yamamoto, M. K., Luce, H., Tabata, Y., Hashiguchi, H., Yamamoto, M., Yamanaka, M. D., and Fukao, S.: Turbulence generation by Kelvin-Helmholtz instability in the tropical tropopause layer observed with a 47 MHz range imaging radar, Journal of Geophysical Research: Atmospheres, 115, https://doi.org/10.1029/2010JD013864, _eprint: https://agupubs.onlinelibrary.wiley.com/doi/pdf/10.1029/2010JD013864, 2010.

Miles, J. W.: On the stability of heterogeneous shear flows, Journal of Fluid Mechanics, 10, 496–508, https://doi.org/10.1017/S0022112061000305, 1961.

Muhammad, F. R., Lubis, S. W., Tiarni, I., and Setiawan, S.: Influence of the Indian Ocean Dipole (IOD) on Convectively Coupled Kelvin and Mixed Rossby-Gravity Waves, IOP Conf. Ser.: Earth Environ. Sci., 284, 012 012, https://doi.org/10.1088/1755-1315/284/1/012012, 2019.

Muñoz-Esparza, D., Sharman, R. D., and Trier, S. B.: On the Consequences of PBL Scheme Diffusion on UTLS Wave and Turbulence Representation in High-Resolution NWP Models, Monthly Weather Review, 148, 4247–4265, https://doi.org/10.1175/MWR-D-20-0102.1, 2020.

Plumb, R. A.: A "tropical pipe" model of stratospheric transport, Journal of Geophysical Research: Atmospheres, 101, 3957–3972, https://doi.org/10.1029/95JD03002, _eprint: https://agupubs.onlinelibrary.wiley.com/doi/pdf/10.1029/95JD03002, 1996.

Podglajen, A., Hertzog, A., Plougonven, R., and Žagar, N.: Assessment of the accuracy of (re)analyses in the equatorial lower stratosphere, Journal of Geophysical Research: Atmospheres, 119, 11,166–11,188, https://doi.org/10.1002/2014JD021849, _eprint: https://agupubs.onlinelibrary.wiley.com/doi/pdf/10.1002/2014JD021849, 2014.

Podglajen, A., Bui, T. P., Dean-Day, J. M., Pfister, L., Jensen, E. J., Alexander, M. J., Hertzog, A., Kärcher, B., Plougonven, R., and Randel, W. J.: Small-Scale Wind Fluctuations in the Tropical Tropopause Layer from Aircraft Measurements: Occurrence, Nature, and Impact on Vertical Mixing, Journal of the Atmospheric Sciences, 74, 3847–3869, https://doi.org/10.1175/JAS-D-17-0010.1, 2017.

Saji, N. H., Goswami, B. N., Vinayachandran, P. N., and Yamagata, T.: A dipole mode in the tropical Indian Ocean, Nature, 401, 360–363, https://doi.org/10.1038/43854, 1999.

Stull, R. B.: Turbulence Kinetic Energy, Stability and Scaling, in: An Introduction to Boundary Layer Meteorology, edited by Stull, R. B., pp. 151–195, Springer Netherlands, Dordrecht, ISBN 978-94-009-3027-8, https://doi.org/10.1007/978-94-009-3027-8_5, 1988.

Thorpe, S. A.: Turbulence and mixing in a Scottish Loch, Philos Trans A Math Phys Eng Sci, 286, 125–181, https://doi.org/10.1098/rsta.1977.0112, 1977.

van Oldenborgh, G. J., Hendon, H., Stockdale, T., L'Heureux, M., Coughlan de Perez, E., Singh, R., and van Aalst, M.: Defining El Niño indices in a warming climate, Environ. Res. Lett., 16, 044 003, https://doi.org/10.1088/1748-9326/abe9ed, 2021.

https://doi.org/10.5194/egusphere-2026-2520
Preprint. Discussion started: 22 May 2026

Vanneste, J. and Haynes, P. H.: Intermittent mixing in strongly stratified fluids as a random walk, Journal of Fluid Mechanics, 411, 165–185, https://doi.org/10.1017/S0022112099008149, 2000.

Vincent, R. A. and Hertzog, A.: The response of superpressure balloons to gravity wave motions, Atmospheric Measurement Techniques, 7, 1043–1055, https://doi.org/10.5194/amt-7-1043-2014, 2014.

Wilson, R., Dalaudier, F., and Luce, H.: Can one detect small-scale turbulence from standard meteorological radiosondes?, Atmos. Meas. Tech., 4, 795–804, https://doi.org/10.5194/amt-4-795-2011, 2011.

Wilson, R., Luce, H., Hashiguchi, H., Dalaudier, F., Fukao, S., Nakajo, T., Shibagaki, Y., Yabuki, M., and Furumoto, J.: Small scale turbulence and instabilities observed simultaneously by radiosondes and the MU radar, in: 13th International Workshop on Technical and Scientific Aspects of MST Radar, Kühlungsborn, Germany, https://hal.science/hal-00815851, 2012.

Wilson, R., Pitois, C., Podglajen, A., Hertzog, A., Corcos, M., and Plougonven, R.: Detection of turbulence occurrences from temperature, pressure, and position measurements under superpressure balloons, Atmospheric Measurement Techniques, 16, 311–330, https://doi.org/10.5194/amt-16-311-2023, 2023.

Woods, J. D.: On Richardson's Number as a Criterion for Laminar-Turbulent-Laminar Transition in the Ocean and Atmosphere, Radio Science, 4, 1289–1298, https://doi.org/10.1029/RS004i012p01289, _eprint: https://agupubs.onlinelibrary.wiley.com/doi/pdf/10.1029/RS004i012p01289, 1969.

Yamamoto, M. K., Fujiwara, M., Horinouchi, T., Hashiguchi, H., and Fukao, S.: Kelvin-Helmholtz instability around the tropical tropopause observed with the Equatorial Atmosphere Radar, Geophysical Research Letters, 30, https://doi.org/10.1029/2002GL016685, _eprint: https://agupubs.onlinelibrary.wiley.com/doi/pdf/10.1029/2002GL016685, 2003.